Advanced Functional Materials

ADVANCED FUNCTIONAL MATERIALS
www.afm-journal.de

RESEARCH ARTICLE

ROS-Responsive Microneedles Loaded With Biomimetic Nanozymes for Rotator Cuff Repair and Adipose Infiltration Prevention

Jintao Li[1,2] | Zhicheng Wen[1,2] | Meimei Fu[3] | Shaozi Zhong[1,2] | Yitao Zhao[1,2] | Zhengnong Wei[4] | Haolin Ke[1,2] | Dianxuan Wu[1,2] | Jiachen Teng[1,2] | Yan Shao[1,2] | Jinshan Guo[2,3,5] | Chun Zeng[1,2]

[1]Department of Sports Medicine, Center For Orthopedic Surgery, The Third School of Clinical Medicine, Orthopedic Hospital of Guangdong Province, Southern Medical University, The Third Affiliated Hospital of Southern Medical University, Guangzhou, P. R. China | [2]Department of Orthopedics, Guangdong Provincial Key Laboratory of Bone and Joint Degeneration Diseases, Academy of Orthopedics Guangdong Province, The Third Affiliated Hospital of Southern Medical University, Guangzhou, P. R. China | [3]Department of Histology and Embryology, NMPA Key Laboratory For Safety Evaluation of Cosmetics, GDMPA Key Laboratory of Key Technologies For Cosmetics Safety and Efficacy Evaluation, School of Basic Medical Sciences, Southern Medical University, Guangzhou, P. R. China | [4]Department of Spine Surgery, Center For Orthopedic Surgery, The Third Affiliated Hospital of Southern Medical University, Guangzhou, P. R. China | [5]CAS Key Laboratory of High-Performance Synthetic Rubber and Its Composite Materials, Changchun Institute of Applied Chemistry, Chinese Academy of Sciences, Changchun, P. R. China

Correspondence: Yan Shao (shaoyan_n@163.com) | Jinshan Guo (jsguo4127@smu.edu.cn) | Chun Zeng (zengdavid@126.com)

Received: 19 June 2025 | **Revised:** 10 May 2026 | **Accepted:** 13 May 2026

Keywords: adipose infiltration | biomimetic nanozymes | metal-polyphenol networks | tendon-bone interface | tendon regeneration

ABSTRACT

The difficulty in tendon-bone interface repair and surrounding muscle adipose infiltration after rotator cuff injuries present significant clinical challenges, necessitating the development of biomaterials capable of repairing the interface and preventing adipose deposition. In this study, we developed a reactive oxygen species (ROS)-responsive microneedle patch (Cu/MnTA-HP) designed to facilitate rotator cuff injuries repair and reduce adipose tissue deposition. Utilizing the natural metal prosthetic groups Cu^{2+} and Mn^{2+} of superoxide dismutase (SOD) enzyme, we coordinated with tannic acid (TA) to form metal polyphenol nanoparticles (Cu/MnTA), which mimic the structure and function of natural SOD enzymes. Subsequently, dynamic covalent boronate ester bonds between Cu/MnTA and phenylboronic acid-modified hyaluronic acid (HP) ensured the microneedles' intelligent response to ROS. The constructed mimetic SOD nanozymes-Cu/MnTA, on the one hand, release TA to eliminate endogenous reactive oxygen, and on the other hand, participate in a series of natural enzymatic reactions (Superoxide dismutase-like, Peroxidase-like), thereby rescuing mitochondrial function (enhancing mitochondrial membrane potential levels and reducing mitochondrial ROS production) in tendon-derived stem cells, promoting tenogenic differentiation, and inhibiting adipose accumulation. This approach promotes the repair of the tendon-bone interface in rotator cuff injuries and reduces fatty infiltration in surrounding muscles.

Jintao Li, Zhicheng Wen and Meimei Fu contributed equally to this work.

1 | Introduction

Rotator cuff injuries, often resulting from improper kinematic patterns during physical activities or age-related degenerative conditions, are prevalent in sports medicine, with an incidence rate as high as 28% [1–3]. This rate escalates to 54% in the population aged over 60 years [4]. Rotator cuff injuries typically require a range of therapeutic interventions to alleviate symptoms and promote tissue repair. The current clinical approaches to managing rotator cuff injuries encompass pharmacotherapy [5, 6], rehabilitative modalities [7, 8], and surgical interventions [9, 10]. Nevertheless, pharmacological and rehabilitative strategies are deemed conservative and fail to address the underlying tendon damage. Surgical intervention represents the principal clinical methodology for resolving rotator cuff injuries, however, it is not without challenges, including the slow healing process at the bone-tendon interface, the risk of tendon re-rupture, and the infiltration of adipose tissue in the affected muscles after surgery [11–13]. Despite the development of various bioactive materials designed to promote healing at the bone-tendon junction, the issue of suboptimal healing due to muscle adipose infiltration persists [14]. Therefore, there is an urgent need to innovate and develop novel biomaterials that can enhance the regeneration of the bone-tendon interface while concurrently inhibiting adipose infiltration, thereby addressing tendon regeneration and preventing adipose infiltration following rotator cuff injuries.

Tissue engineering represents a novel avenue for the regeneration of the tendon-bone interface and the prevention of postoperative complications. Hydrogel materials, engineered scaffolds, or tissue patches are typically employed as the main components in repairing rotator cuff injuries [15–17]. However, the constrained application techniques of hydrogel materials and the bio-inertness of engineered scaffolds and tissue patches impede their clinical use. Despite the development of a range of bioactive materials to facilitate the healing of the bone-tendon interface, the issue of fatty infiltration in the supraspinatus muscle during the healing process appears to be neglected [18]. In addition, the challenges arising from local inflammatory environments and those associated with tendon regeneration must be adequately addressed. Therefore, the design of a biomaterial for the repair of rotator cuff injuries must incorporate functions that modulate the bone microenvironment, promote tendon regeneration, and inhibit adipose infiltration. Such a locally applied bio-regulatory material can release drugs in response to microenvironmental stimuli, foster tendon regeneration, and prevent fatty infiltration, thereby enhancing the quality of rotator cuff repair.

Tendon regeneration is crucial for repairing rotator cuff injuries. This process involves not only the healing of the tendon-bone interface but also the regulation of growth factors, the application of biological methods, and the development of functional integrated regenerative technologies. Evidence indicates that mitochondrial damage caused by reactive oxygen species (ROS) is the primary impediment to the maturation of tendon-derived stem cells (TDSCs) into fully differentiated tenocytes [19, 20]. Specifically, the accumulation of extrinsic ROS compromises the mitochondria of TDSCs, culminating in a decrement of mitochondrial membrane potential and an accrual of mitochondrial ROS, which in turn further impairs the differentiation of TDSCs [21]. Simultaneously, the dysregulation of mitochondrial functionality in muscular cells can also precipitate adipose accumulation within the muscles of the rotator cuff [22]. Previous studies have indicated that superoxide dismutase (SOD), an antioxidant metalloenzyme present in biological systems, plays a crucial role in the balance of oxidative and antioxidative processes and in stabilizing mitochondrial function by catalyzing the dismutation of superoxide anion radicals into oxygen and hydrogen peroxide [23, 24]. Consequently, we have engineered a nanozyme with mimetic SOD enzymatic activity. By emulating the natural enzymatic function, this nanozyme regulates local inflammatory responses, thereby restoring the mitochondrial functionality of TDSCs and curbing adipose deposition.

Tannic acid (TA), a potent free radical scavenger found in plants, exhibits anti-inflammatory, anti-aging, antioxidant, and antibacterial properties [25]. However, its clinical application is limited by low bioavailability and the lack of controllable release characteristics. Our previous research developed a metal-polyphenol system through the interaction between metal ions and polyphenols, which not only preserved the biological effects of polyphenols but also achieved synergistic slow release of metal ions and polyphenols, and has been applied in the field of bone and cartilage regeneration [26, 27]. Based on this, we aim to design a biomimetic SOD enzyme by introducing natural metal prosthetic groups Cu^{2+} and Mn^{2+}, which combine with the pyrogallol structure of TA, to form biomimetic SOD enzyme particles (Cu/MnTA) capable of modulating inflammation and simulating multiple enzymatic activities [28]. Cu^{2+} and Mn^{2+} serve as metal ligands for TA, which not only preserve the characteristics of TA but also mimic the structure and composition of SOD enzymes, regulating the inflammatory microenvironment, stabilizing mitochondrial function, and ultimately promote healing at the bone-tendon interface while inhibiting pathological fatty infiltration.

In this study, we developed a hydrogen peroxide (H_2O_2)-responsive microneedle patch (HP) by loading the previously synthesized biomimetic SOD enzyme (Cu/MnTA) into a crosslinked polymer gel and evaluated its therapeutic effect upon implantation in the supraspinatus tendon (Scheme 1). The dynamic covalent boronic ester linkages between TA and phenylboronic acid-modified hyaluronic acid (HP) constitute the microneedle polymer gel (Cu/MnTA-HP). Hydrogen bonding interactions further enhance the high loading capacity of TA within the gel. The Cu/MnTA is conjugated to HP via dynamic covalent boronate ester bonds that selectively cleave in a high-ROS microenvironment. This ROS-responsive dissociation enables the intelligent, on-demand release of the nanozymes, allowing them to participate in the regulation of local inflammatory responses. The released Cu/MnTA nanozyme, on the one hand, releases TA to inhibit inflammation and provide a favorable environment for bone and tendon healing. On the other hand, as a biomimetic SOD enzyme, it participates in a series of natural enzymatic reactions (Superoxide dismutase-like, Peroxidase-like), rescuing mitochondrial function in tendon-derived stem cells, thereby promoting tendon differentiation and inhibiting adipose accumulation. Therefore, this microneedle patch, loaded with biomimetic nanozymes, represents a novel delivery system that integrates material properties with bio-therapeutics.

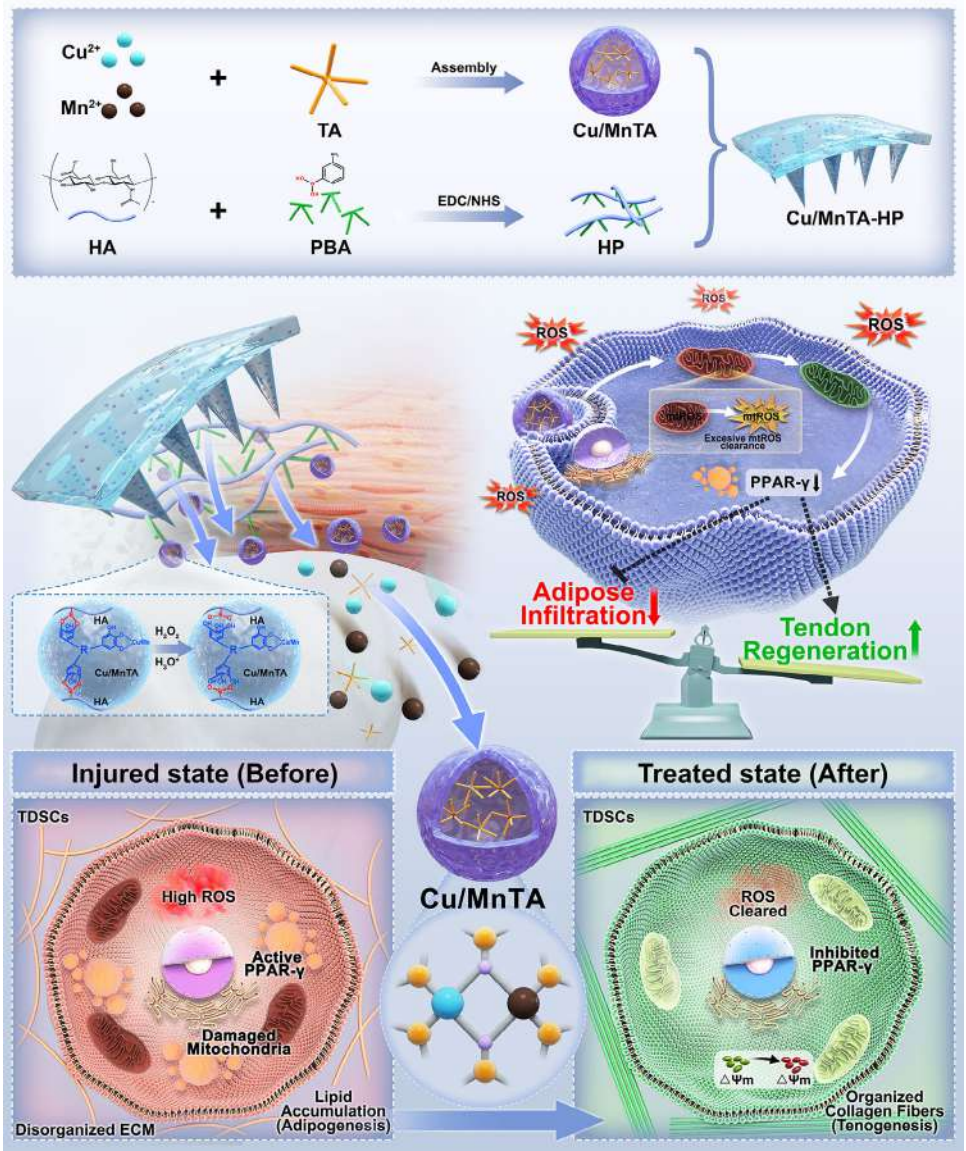

SCHEME 1 | Schematic synthesis of microneedle loaded with bionic SOD-like nanozymes. This microneedle allows localized release of bionic nanozymes to promote bone-tendon interface repair by modulating the inflammatory environment and improving mitochondrial function in TDSCs.

2 | Results

2.1 | Synthesis and Characterizations of CuTA, MnTA and Cu/MnTA Nanozymes

As shown in Figure 1A, CuTA, MnTA, and Cu/MnTA were successfully synthesized by a one-step method. The morphology of CuTA, MnTA, and Cu/MnTA was revealed by SEM analysis (Figure 1B). Among them, the size of CuTA is similar to that of MnTA (50–100 nm), while the size of Cu/MnTA becomes significantly larger (300–500 nm) than that of the monometallic coordination after introducing both metal ions. Moreover, the element mapping images of Cu/MnTA (Figure S2, Supporting Information) further confirm the successful inclusion of TA in Cu/MnTA and showcase the uniform distribution of Cu^{2+} and Mn^{2+} within the Cu/MnTA structure. Additionally, Figure S3 presents the elemental composition of three types of nanoparticles as observed under scanning electron microscopy. As demonstrated in the SEM images, particle size analysis revealed that the average particle diameters of CuTA and MnTA are approximately 64.84 and 76.04 nm, respectively, while the average particle diameter of Cu/MnTA reaches 381 nm (Figure S4). The successful introduction of TA was confirmed by the presence of characteristic peaks at 1479 cm^{-1} in the FTIR spectra of the three nanoparticles [29] (Figure 1C). The show-up of both the peaks of O (533.1 eV) and C (288.1 eV) from TA, as well as the X-ray photoelectron spectroscopy (XPS) of Cu/MnTA with Cu (934.8 eV) and Mn (642.0 eV) peaks (Figure 1D), confirmed the successful synthesis of Cu/MnTA [30, 31]. Thermogravimetric analysis (TGA) indicates that, under controlled heating conditions, the mass loss of Cu/MnTA was approximately 65% at temperatures up to 1000°C (Figure 1E). Also, the XRD image of TA, CuTA, MnTA, and Cu/MnTA was showed in Figure S5. These results confirm the successful incorporation of organic components, with an approximate mass ratio of organic to inorganic of 2:1, and demonstrate that the thermal stability of

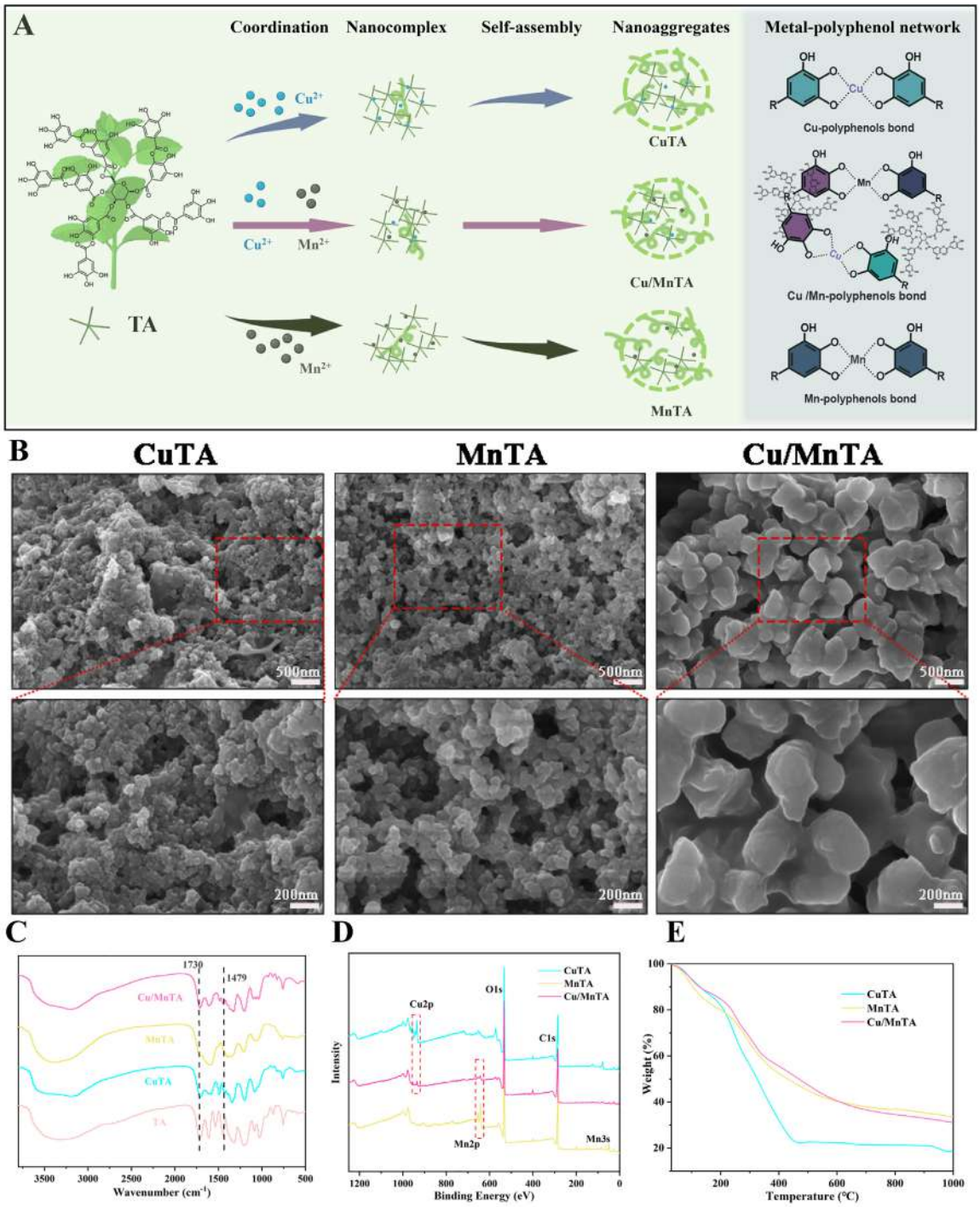

FIGURE 1 | Schematic synthesis and characterization of three nanozymes. (A) Schematic synthesis of nanozymes by one-step self-assembly. (B) Scanning electron microscopy (SEM) patterns of the nanozymes. Fourier transform infrared (FTIR) spectra (C) of TA, CuTA, MnTA, and Cu/MnTA, and XPS wide scans (D) and TGA curves (E) of CuTA, MnTA, and Cu/MnTA.

Cu/MnTA is enhanced compared to CuTA when both metal ions are considered.

2.2 | Cellular Viability, Proliferation, Migration and Superoxide Dismutase Activity of Nanozymes

The cell compatibility of three types of nanoparticles was assessed using the cell counting kit 8 (CCK-8) assay and Live/Dead staining kit. As can be seen from Figure 2A,B and Figure S6B, none of the CuTA groups showed significant toxicity when the concentration was < 240 μg/mL. While CuTA at concentrations > 500 μg/mL induced significant toxicity with cell survival < 50%. In addition, MnTA exhibited poor cytocompatibility. At a concentration of 30 μg/mL, the cell survival rate in the MnTA group was about 75%. However, in the Cu/MnTA group where both metal ions were introduced, the cytotoxicity exhibited similar cytotoxicity to that of the CuTA group. The cell survival rate in

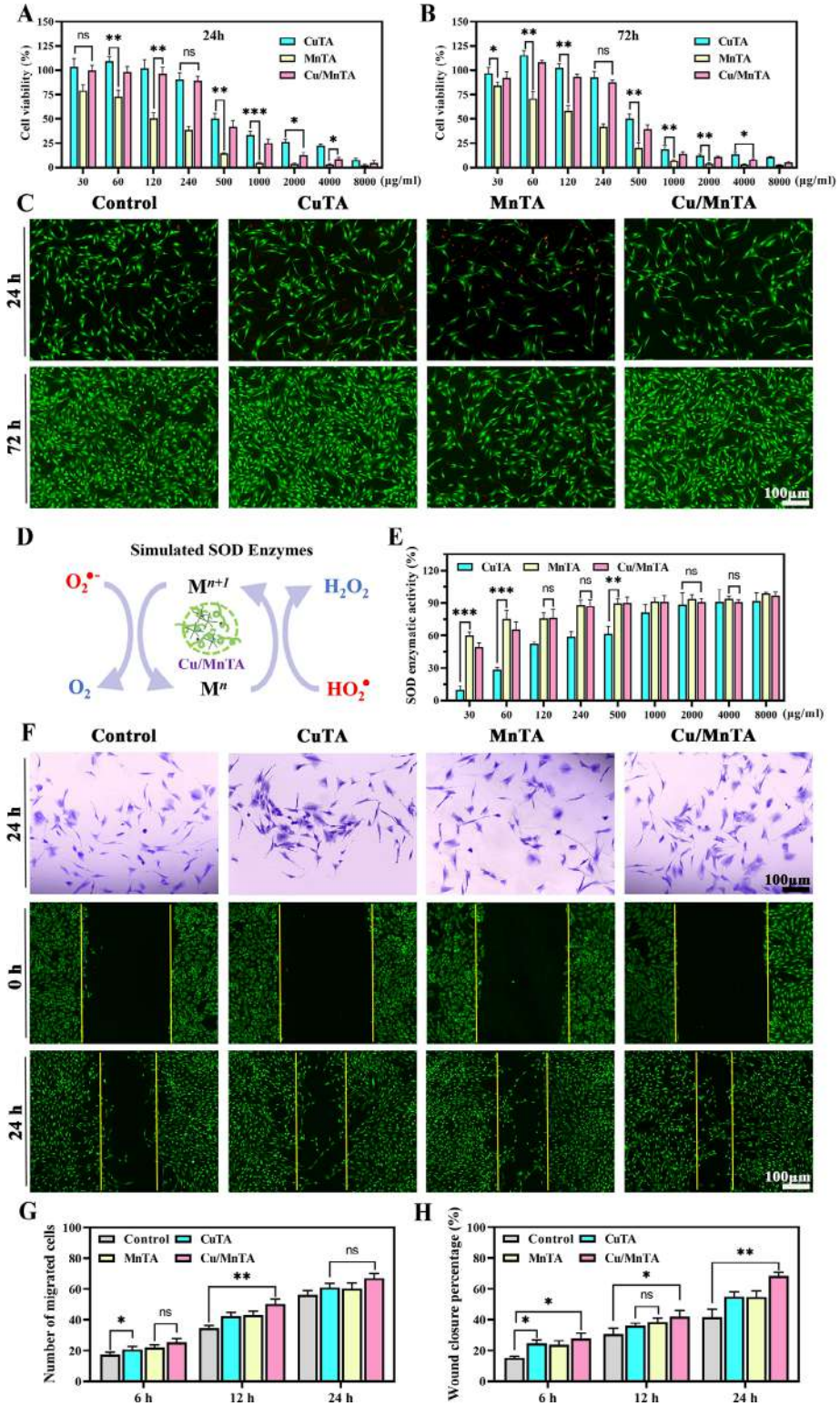

FIGURE 2 | In vitro cytocompatibility, migration properties and superoxide dismutase characterization assays of nanozymes. CCK-8 assay at different concentrations of the three nanozymes at 24 h (A) and 72 h (B) (n = 3). (C) Live/dead images of TDSCs treated with different nanozymes at 240 μg/mL for 24 and 48 h (representative images). (D) SOD enzyme mechanism of action diagrams and SOD enzymes activity assay (E) of CuTA, MnTA, and Cu/MnTA simulations (n = 3). (F) Transwell images and cell migration images at 24 h (representative images). (G) Migration rate quantification of transwell images (n = 3). (H) Cell migration related quantitative data obtained from scratch assay (n = 3). *$p < 0.05$, **$p < 0.01$, ***$p < 0.001$,"ns" represents no significant difference.

the Cu/MnTA group was about 85% when the concentration was < 240 μg/mL. This indicated that compared with Mn^{2+}, Cu^{2+} had lower cytotoxicity and was effective in maintaining cell survival in the mixed system of bimetallic ions. The Live/Dead staining images in Figure 2C and Figure S6A support these findings, confirming the good cytocompatibility of Cu/MnTA, making it a promising candidate for in vivo applications. As shown in Figure S7, NBT will be reduced to blue NBT formamide by $\cdot O^{2-}$, and its absorption increases in UV-visible experiments. Also, we used natural polyphenol tannic acid (TA) and three types of nanozymes to detect SOD enzyme activity. The results shown in the following figure indicate that compared with the TA and CuTA groups, the Cu/MnTA group exhibits excellent biomimetic SOD enzyme activity, and its effect is close to that of the MnTA group (Figure S8). After adding nanozymes to the system, superoxide anions can be quickly removed, thereby preventing the reduction of NBT and resulting in low UV absorbance at 560 nm. As shown in Figure 2E, both CuTA and MnTA have superoxide scavenging activity, but MnTA exhibits better ability to scavenge superoxide anions. At a concentration of 240 μg/mL, the SOD inhibition rate of MnTA could reach about 90%. It can still maintain high superoxide scavenging activity at a Cu/MnTA concentration of 240 μg/mL.

Also, as shown in the Figure S9, the superoxide anion ($\bullet O_2^-$) scavenging capacity of tannic acid (TA) and the Cu/MnTA nanozyme was compared using DMPO as the spin trap. As the organic precursor of the nanozyme and a known antioxidant, TA exhibited a measurable level of $\bullet O_2^-$ scavenging ability, which is consistent with the radical-reducing property of its polyphenolic structure. In contrast, the Cu/MnTA nanozyme significantly reduced the characteristic DMPO/$\bullet O_2^-$ signal, displaying a markedly lower EPR signal intensity compared to that of TA alone. Based on the cytotoxicity of Cu/MnTA, we chose a concentration of 240 μg/mL for further research. The mechanism of Cu/MnTA simulating superoxide dismutase activity is shown in Figure 2D. In addition, the effect of Cu/MnTA on TDSCs migration was assessed by transwell and cell scratch assays. Figure S10A summarizes the transwell assay, Figure 2F,G and Figure S10B demonstrates the longitudinal cell migration. The migration rate in the Cu/MnTA group was significantly higher than in the control group. Figure 2F,H and Figure S10B, illustrating the cell scratch test assessing lateral cell migration, further confirmed the increased migration rate in the Cu/MnTA group (approximately 70% after 24 h) compared to the control group (approximately 40% after 24 h). This indicated that Cu/MnTA enhanced cell migration and proliferation. These findings emphasize the good cytocompatibility of Cu/MnTA and its great potential in promoting cell proliferation and migration, which facilitates its application in tendon-bone healing.

2.3 | Experiments of Enzyme-Like Activity

Rotator cuff injuries usually trigger a localized inflammatory response, leading to the production of ROS (Reactive Oxygen Species) in the microenvironment and impeding the regeneration of the bone-tendon interface [32]. Given the excellent antioxidant capacity of tannic acid (TA) containing abundant phenolic groups, we characterized the antioxidant performance of nanozymes. Therefore, we investigated the antioxidant capacity of Cu/MnTA using the 2,2-diphenyl-1-trinitrophenylhydrazine (DPPH) kit. As shown in Figure 3A, the DPPH radical solution begins to turn purple, and its color varies depending on the type or duration of the nanozyme added. TA has numerous phenolic hydroxyl groups, which can provide sufficient electrons to reduce DPPH. Figure 3B,C shows that after 5 min, the DPPH absorption intensity at 517 nm in the Cu/MnTA group was significantly reduced by about 40% compared to the control group. When the treatment was extended to 30 min, the DPPH clearance rate reached approximately 81.2% (Figure 3D,E).

The peroxidase-like activity of Cu/MnTA was assessed by oxidizing the substrate TMB to oxTMB in the presence of hydrogen peroxide. The peroxidase-like activity of Cu/MnTA was spectrally evaluated using 3,3',5,5'-tetramethylbenzidine (TMB) and H_2O_2 as substrates. Cu/MnTA oxidizes TMB to ox-TMB, resulting in the solution's color shifting from colorless to blue (Figure 3F). TA, CuTA, MnTA, and Cu/MnTA all display absorption peaks at 650 nm, indicating their peroxidase-like activity (Figure 3G). However, MnTA showed lower peroxidase-like activity, whereas Cu/MnTA significantly enhanced performance. Figure 3H illustrates the absorption peak curve of Cu/MnTA in the TMB solution over time. In addition, we evaluated the peroxidase-like catalytic performance of Cu/MnTA using *o*-phenylenediamine (OPD) and H_2O_2 (Figure S11A). Similarly, all three nanozymes exhibited absorption peaks at 432 nm (Figure S11B). Among them, CuTA exhibits the best peroxidase-like catalytic performance, while the catalytic activity of Cu/MnTA is significantly improved compared to MnTA's poorer catalytic activity. As time increases, the adsorption peak of Cu/MnTA at 432 nm enhances, demonstrating the time-dependent peroxidase-like activity of Cu/MnTA (Figure S11C). DCFH-DA assay reagent was used to detect total ROS levels. In the presence of H_2O_2, TDSCs produced significantly more ROS compared to the control group. Notably the three nanozymes intervened with significantly lower intracellular ROS levels (Figure 3J). The quantitative fluorescence intensity results in Figure 3I further support this result. These findings confirm that Cu/MnTA could rescue the increased ROS production caused by H_2O_2 and create a favorable microenvironment for tendon bone interface regeneration.

2.4 | Characterization of Microneedles

Synthesize HP by linking 3-Aminophenylboronic acid hydrochloride (PBA) with hyaluronic acid (HA) through amide bonds [33]. Here, HA was chosen due to its excellent biocompatibility and wide application in orthopedic diseases. PBA was selected as the grafting group due to its lower pKa, which enables the formation of boron ester bonds at physiological pH. We formed MNs polymer gel through dynamic covalent boron ester bond between TA in Cu/MnTA system and phenylboronic acid modified hyaluronic acid (HP). The FT-IR spectra of HA and HP demonstrate the successful conjugation of PBA with HA polymer chains (Figure S12A). The peak at 1609 cm^{-1} was assigned to the C═O vibration of ─COOH of HA. The absorption of 1561 and 1366 cm^{-1} in HP were assigned to C═O vibration of ─CONH─ and B─O vibration of PBA, respectively [34, 35]. The ^1H NMR result also revealed the successful conjugation of PBA to HA polymer, with peaks appearing at 7.0–8.0 and 2.0 ppm belonging to benzene rings of PBA and methyl groups of HA, respectively (Figure S12B). Next,

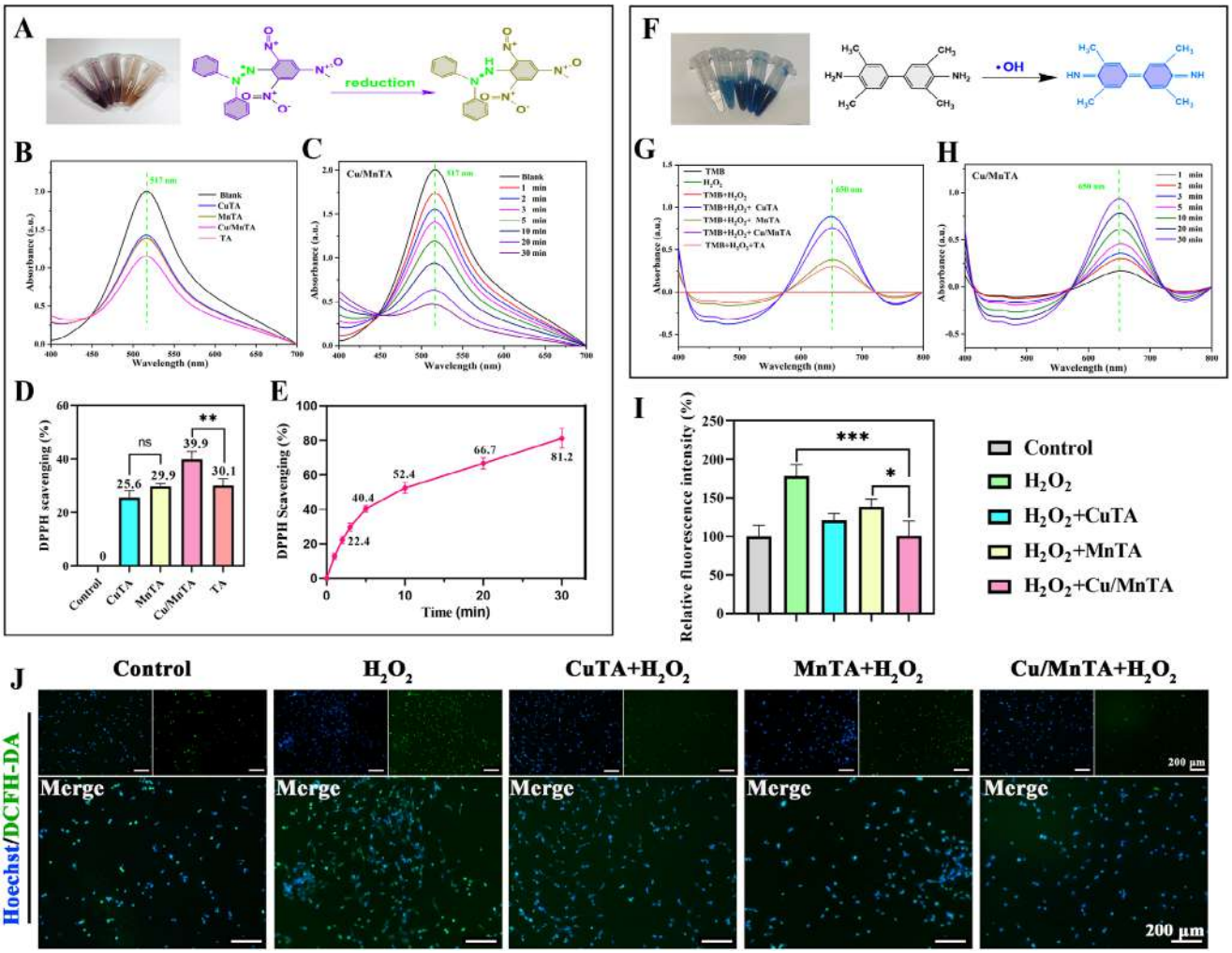

FIGURE 3 | Antioxidant and peroxidase properties of three nanozymes. (A) Photographs of DPPH solutions at different times and schematic diagram of the DPPH radical reduction reaction. (B) UV-vis spectra of different treatments. (C) UV-vis spectral changes of DPPH solutions treated with Cu/MnTA at different times. (D) DPPH scavenging rate (n = 3). (E) UV-vis curve of Cu/MnTA. (F) Photograph of TMB solutions at different times and the schematic diagram of peroxidase activity detected by TMB. (G) UV-visible spectra of different treatments. (H) Changes in UV-visible spectra of Cu/MnTA-treated TMB solutions at different times. (J) Fluorescence images (representative images) and (I) relative fluorescence intensities of oxidation inhibition obtained by ROS test kit on TDSCs (n = 3). $^{*}p < 0.05$, $^{***}p < 0.001$.

HP was mixed with three previously prepared nanozymes (CuTA, MnTA, and Cu/MnTA) to prepare ROS-reactive gels (CuTA-HP, MnTA-HP, and Cu/MnTA-HP). The three ROS-reactive gels showed a broader IR band between 3000~3500cm^{-1} than HP, which was assigned to O—H stretching vibration, indicating the presence of polyphenols in the gel network (Figure S12A).

Here, we fabricated microneedle patches loaded with nanozymes. Figure 4A shows the schematic diagram of the preparation process, and the morphology of DMN obtained by demolding is a neatly arranged array of 15 × 15 microneedles. Figure 4B shows images of the PDMS mold and the loaded nanozyme microneedles after demolding. Figure 4C shows the SEM image of DMN loaded with Cu/MnTA (Cu/MnTA-HP). The tip of the needle is pyramid shaped, complete, uniform, and sharp, with a height of about 700 μm. Moreover, the element mapping images of Cu/MnTA-HP (Figure 4D) further showcase the uniform distribution of Cu^{2+} and Mn^{2+} within the Cu/MnTA-HP. The shaped MNs have sharp tips (Figure S13A). After applying DMN to the pig skin for 2 min, remove it. As shown in Figure S13B, the skin exhibits well-aligned microporous channels. The images in Figure S14 demonstrate the penetration capability of the microneedles into muscle tissue (Figure S14A) and verify their in vivo placement at the surgical site via fluorescence (Figure S14B). Additionally, mechanical property tests were performed on the microneedles. Figure 4E,F show the images of compression tests. Figure 4G displays the force-displacement curve. The maximum failure force of the entire microneedle array with HA or HP is about 6N, with the maximum failure force calculated at 0.027N/needle. However, after the incorporation of nanozymes, the fracture strength of the three types of microneedles (CuTA-HP, MnTA-HP, and Cu/MnTA-HP) significantly increased to approximately 20N, with the maximum failure force calculated at 0.09N/needle (Figure 4H).

To study the ROS-response characteristics of the three gels, we incubated the microneedles in PBS buffer solution with pH 7.4 and different H_2O_2 concentrations (0, 0.2, 0.5, and 1 mM).

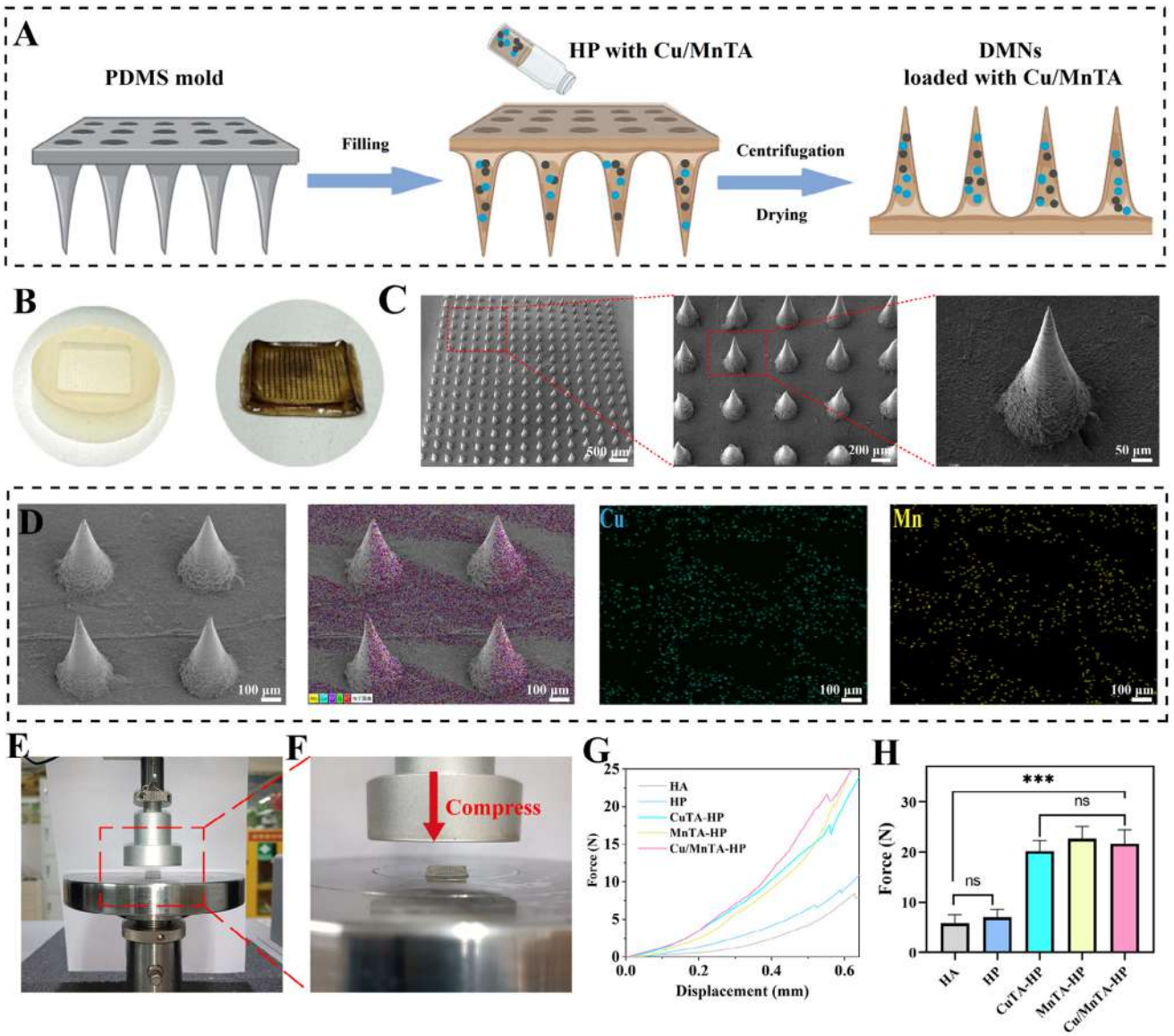

FIGURE 4 | Morphological and mechanical characteristics of microneedles loaded with nanozymes (HP-CuTA, HP-MnTA, and HP-Cu/MnTA). (A) Fabrication process diagram of microneedles. (B) Optical bright-filed images of microneedles and (C) SEM images of the MN tips of the microneedles at different magnifications. (D) SEM images and mapping images of the microneedles. (E&F) Mechanical compression test of the microneedle tip. (G) The force-displacement curves of different microneedles. (H) Axial fracture force of different microneedles (n = 4). ***$p < 0.001$, "ns" represents no significant difference.

The comparative dissolution kinetics of the three microneedle formulations were assessed under physiologically relevant conditions. When immersed in a PBS buffer (pH 7.4) supplemented with 0.5 or 1 mM hydrogen peroxide (H_2O_2), all microneedle types exhibited a similar trend, achieving near-complete dissolution by the 96-h mark. In contrast, microneedles incubated in PBS devoid of H_2O_2 demonstrated negligible dissolution, indicating that the presence of H_2O_2 is a critical factor influencing the dissolution rate of these microneedle constructs (Figure S15). This finding underscores the importance of the local oxidative environment in modulating the degradation profile of the microneedles, which has implications for their potential application in controlled drug delivery and therapeutic interventions. The TA release of Cu/MnTA-HP is calculated based on the TA standard curve using UV absorbance (Figure S16A). Incubation of Cu/MnTA-HP in the presence of H_2O_2 solution increased the rate of TA release. At 14 days, the release of TA from the solution without H_2O_2 was about 70%, which was significantly lower than the release from the solution with 1.0 mM of H_2O_2 (about 90%), demonstrating high sensitivity to H_2O_2 (Figure S16B).

2.5 | Cu/MnTA-HP Inhibited Adipogenic Differentiation and Promoted Tendon Regeneration Under Oxidative Stress In Vitro

During the healing process of rotator cuff injuries, there's often accompanying adipose infiltration into the surrounding muscles, which greatly affects the healing of the bone-tendon interface [36]. Previous studies have found that hydrogen peroxide (H_2O_2)

could simulate an oxidative stress environment, leading to the adipose accumulation and inhibiting the tendon differentiation of TDSCs [37]. In previous rotator cuff injury studies, embryonic fibroblasts (3T3-L1) have been widely recognized in the study of adipogenic differentiation. Here, we use microneedles composed of Cu/MnTA with multiple enzyme-like abilities and ROS scavenging properties to explore whether they can inhibit adipogenic differentiation of 3T3-L1 cells and reduce the inhibitory the tenogenic differentiation potential of TDSCs in the presence of H_2O_2. Figure 5A shows the characteristics of Cu/MnTA-HP in promoting tendon regeneration under oxidative stress environment. As shown in Figure 5B, the lipid droplets formed by cell adipogenic differentiation were stained red. We observed that the size and quantity of lipid droplets in the experimental group were lower than those in the control group and H_2O_2 group (Figure 5C). The immunofluorescence staining images of PPAR-γ also showed similar results (Figure 5B and Figure S17). The qPCR results showed that Cu/MnTA-HP loaded with nanozymes had a strong ability to inhibit adipogenic differentiation, significantly reducing the expression levels of adipogenic-related genes PPAR-γ, CEBP-α, and FABP4 (Figure 5D–F). In addition, there was no significant difference in the inhibition of lipidation between the CuTA-HP group and MnTA-HP group, but the Cu/MnTA-HP group performed better than the other groups.

Tendon regeneration plays a crucial role in the healing process of the tendon bone interface [21]. Scleraxis (SCX) is a tendon-derived transcription factor that is crucial for tendon lineage differentiation [38]. Besides, Tenomodulin (TNMD) is a tendon specific biomarker that supports self-renewal of TDSCs [39]. In addition, type I collagen (Col I) is the main component of the extracellular matrix synthesized by TDSCs in normal tendons [40]. We conducted a semi quantitative study on the expression of these three components in TDSCs by Cu/MnTA-HP in the presence of H_2O_2 using immunofluorescence staining. Cellular immunofluorescence showed that Cu/MnTA-HP could alleviate the inhibitory effect of H_2O_2 on TDSCs expression of SCX, TNMD, and Col I (Figure 5G; Figure S18), which may help improve tendon repair at the tendon-bone interface. Corresponding fluorescence quantification further substantiated these results (Figure 5H–J).

In addition, we validated the expression of tendon-specific markers at the transcriptional level. The qPCR results showed significant differences in Cu/MnTA-HP compared to other groups (Figure 5K–M). The relative RNA expression level of SCX in the H_2O_2+Cu/MnTA-HP group increased from 0.44 in the H_2O_2 group to 1.09 ($P < 0.001$), the relative RNA expression level of TNMD increased from 0.39 in the H_2O_2 group to 1.19($p < 0.001$). The relative RNA expression level of MKX was also restored. These results indicated that Cu/MnTA-HP can alleviate the tendon phenotype inhibition of TDSCs under oxidative stress, which may help promote tendon regeneration at the tendon-bone interface. These findings, together with the suppression of adipogenic markers (PPAR-γ, CEBP-α, FABP4), suggest that Cu/MnTA-HP shifts the cell fate of TDSCs away from adipogenesis and toward tenogenesis, likely through preservation of mitochondrial function and consequent downregulation of PPARγ signaling.

During the repair process of the tendon bone interface, regenerated tissue typically transitions from chondrogenesis to osteogenesis. Therefore, the establishment of the tendon bone interface depends on the osteogenic differentiation of bone marrow stem cells. After co-culturing with TDSCs for 7 days, the fluorescence intensity of RUNX2 and ALP in bone marrow stromal cells was significantly higher in the three microneedle groups than in the control group (Figure S19A). Subsequently, our qPCR results for RUNX2, Col I, and ALP (Figure S19B–D) further confirmed the ability of microneedles to induce osteogenic gene expression. This was consistent with the results of immunofluorescence staining. We speculate that this may be attributed to the osteogenic-promoting effects of metal ions (Cu^{2+} and Mn^{2+}).

2.6 | Cu/MnTA-HP Reduced ROS Levels, Maintained ATP Levels and Mitochondrial Function of TDSCs

The inflammatory environment often affects cellular physiological functions, including energy metabolism [41]. Mitochondria is the main organelle for energy metabolism, and the environment with excessive ROS would affect mitochondrial function, including a decrease in mitochondrial membrane potential levels and excessive production of mtROS (Figure 6A) [42]. Therefore, we evaluated the effect of Cu/MnTA nanozyme on the ATP levels of TDSCs using an ATP detection kit. It was found that the nanozyme successfully restored ATP production to a certain extent (Figure 6B, H_2O_2 vs H_2O_2+Cu/MnTA-HP, 0.48 vs 0.74, $p < 0.01$). Moreover, the relative DCFH-DA fluorescence intensity of the H_2O_2+Cu/MnTA-HP group was significantly lower than that of the H_2O_2 group (Figure 6C), reflecting the decrease in ROS level in TDSCs. The massive accumulation of ROS could alter the membrane potential of mitochondria, leading to an energy crisis in TDSCs. Using the JC-1 probe to measure mitochondrial membrane potential. The immunofluorescence results showed that the H_2O_2 group had significant JC-1 monomers, while the H_2O_2+Cu/MnTA-HP group could greatly stabilize the mitochondrial membrane potential (Figure 6D; Figure S20A). In addition, we used MitoSox mitochondrial superoxide indicator to verify the changes in mitochondrial ROS, and the results were consistent with the JC-1 probe (Figure 6E; Figure S20B). Furthermore, TEM imaging provided direct visual evidence for the preservation of mitochondrial structural integrity. As shown in the Figure S21, H_2O_2 treatment induced obvious mitochondrial swelling with blurred or disrupted cristae—a classic hallmark of oxidative damage. In contrast, cells treated with Cu/MnTA-HP exhibited intact mitochondrial morphology with clearly defined and densely packed cristae, similar to the normal control group. This provides direct evidence at the subcellular structural level that our nanozyme system effectively protects mitochondria from oxidative injury, thereby maintaining the structural foundation necessary for their normal function. These results indicated that Cu/MnTA-HP can alleviate mitochondrial functional damage caused by H_2O_2, including membrane potential reduction and mtROS increase.

To analyze the causal hierarchy of Cu/MnTA HP effects, we performed additional intervention experiments using the mitochondrial complex I inhibitor Rotenone, the PPARγ agonist

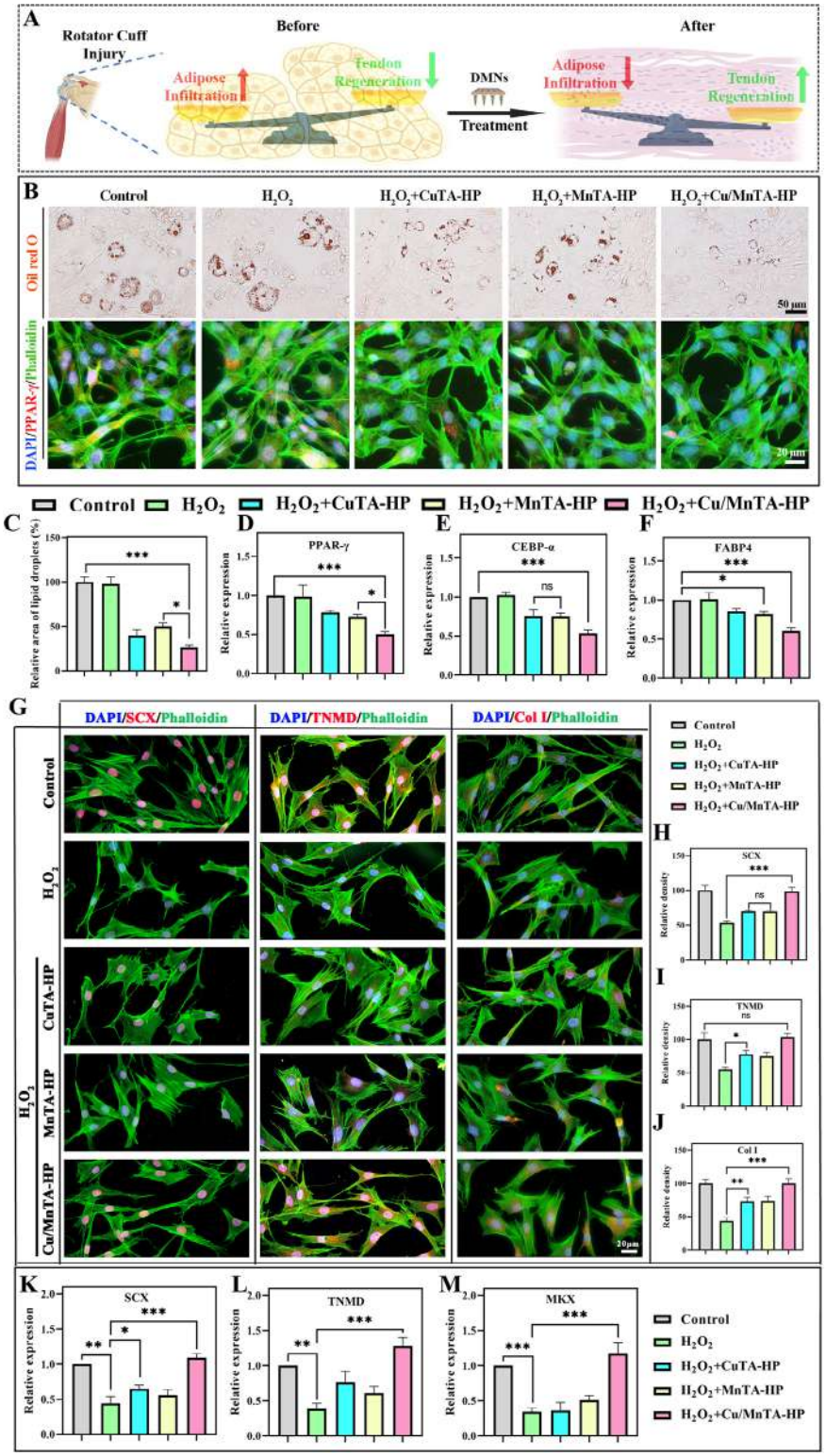

FIGURE 5 | Microneedles loaded with nanozymes inhibited fatty accumulation and promoted tendon regeneration. (A) Schematic diagram of the microneedles inhibited fatty accumulation and promoted tendon regeneration. (B) Oil red O staining and PPAR-γ immunofluorescence staining images of 3T3-L1 cells treated with different microneedles after 10 days of induction (representative images). (C) Quantitative data of oil red O staining (n = 3). (D,E,F) qPCR measurements of gene expression of PPAR-γ, CEBP-α, and FABP4 after induction of TDSCs by different microneedles for 7 days (n = 3). (G) Immunofluorescence staining of SCX, TNMD, and Col I of TDSCs with different microneedle interventions (representative images). (H,I,J) Quantification of immunofluorescence staining of SCX, TNMD, and Col I, respectively (n = 3). (K,L,M) qPCR measurements of gene expression of SCX, TNMD, and MKX, respectively (n = 3). *$p < 0.05$, **$p < 0.01$, ***$p < 0.001$,"ns" represents no significant difference.

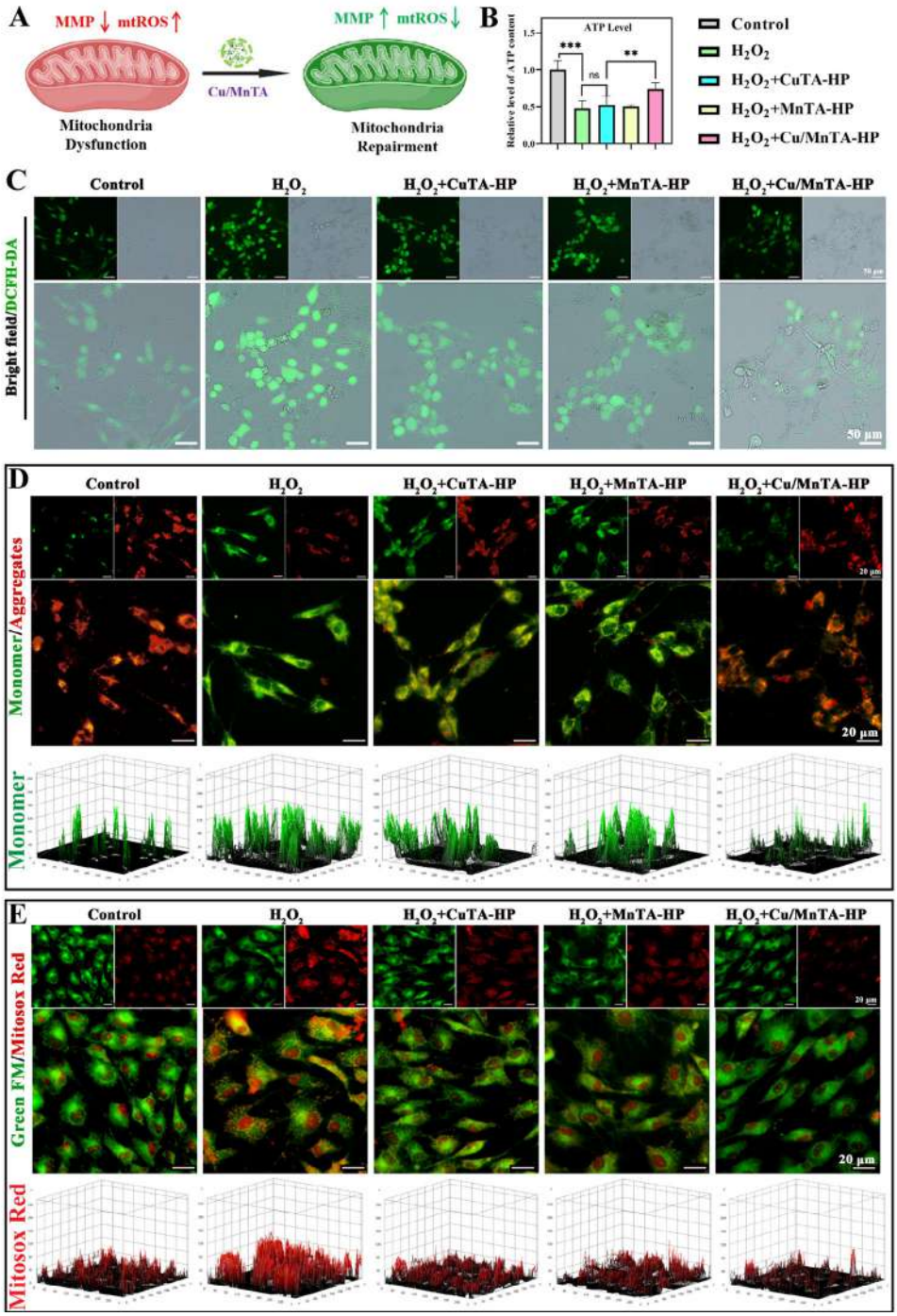

FIGURE 6 | Cu/MnTA-HP maintained ATP levels, alleviated H_2O_2-induced oxidative stress, and restored mitochondrial membrane potential of TDSCs in vitro. (A) Schematic representation of the effect of Cu/MnTA-HP on mitochondrial damage. (B) Estimation of cellular ATP level after 6 h of H_2O_2-induced oxidative stress in the presence or absence of MNs (n = 3). (C) Immunofluorescence staining images of intracellular ROS detected using the DCFH-DA probe (representative images). (D) Immunofluorescence staining images of mitochondrial membrane potential (ΔΨm) were detected using the JC-1 probe (representative images). (E) Immunofluorescent staining images of mitochondrial superoxide detected by Mitotracker indicator and Mitosox Red indicator (representative images). $^{**}p < 0.01$, $^{***}p < 0.001$,"ns" represents no significant difference.

Rosiglitazone (RSG), and the broad-spectrum antioxidant NAC (Figure S22). As shown in Figure S22A–C, Rotenone completely abolished the Cu/MnTA-HP-induced reduction of ROS, restoration of ATP levels, and suppression of PPAR-γ protein expression, indicating that mitochondrial function integrity is an upstream requirement for the nanozyme's effects. In contrast, NAC partially recapitulated the ROS scavenging and PPAR-γ inhibition but was less effective than Cu/MnTA-HP, suggesting that the nanozyme provides additional direct mitochondrial protection beyond mere antioxidant activity. Furthermore, activation of PPAR-γ by RSG reversed the pro-tenogenic effects of Cu/MnTA-HP, as evidenced by decreased SCX and TNMD expression in both western blot and immunofluorescence assays (Figure S22D–F). These data collectively establish that mitochondrial protection

lies upstream of PPAR-γ inhibition, and that downregulation of PPAR-γ is a mechanistic requirement – not merely a downstream consequence – for the therapeutic effect of Cu/MnTA-HP on tenogenic differentiation.

2.7 | In Vivo Study of Rat Rotator Cuff Tears (RCT) Model

Regeneration of tendon tissue is crucial during the repair of the tendon-bone interface. Bone tissue remodeling at the tendon insertion site plays an irreplaceable role. These two processes are interconnected in both the physiological context and the temporal sequence [43]. After establishing a randomized controlled trial model in rats, we fixed CuTA-HP, MnTA-HP, and Cu/MnTA-HP at the distal end of the supraspinatus tendon (proximal to the bone tendon junction). In addition, we included a blank group (simple suture group) as a control. We evaluated the efficacy of these microneedles in repairing rotator cuff injuries in rats through bone volume analysis, finite element analysis, mechanical analysis, and histological analysis (Figure 7A).

2.8 | Micro-CT Analysis, Biomechanical Testing and Finite Element Analysis

At 2, 4, and 8 weeks after surgery, we collected the shoulders of rats for micro-CT analysis. As shown in Figure 7B (including 3D visualization and coronal section images), three groups implanted with microneedles showed superior morphology of the healing interface at postoperative weeks 4 and 8 compared with the Control group, especially the Cu/MnTA-HP group. In addition, at 8 weeks, the morphology of the healing interface was smoother in the Cu/MnTA-HP group, confirming its good effect of promoting bone tissue remodeling. The statistical analysis results of subchondral bone morphology parameters are shown in Figure 7C–E. The bone density, and bone volume fraction of the Cu/MnTA-HP group were higher than those of the other groups ($P<0.05$). At the same time, the analysis of trabecular separation rate in each group showed that the Cu/MnTA-HP group had the lowest incidence rate. These results indicate that local implantation of Cu/MnTA-HP significantly improves the osteogenic properties of subchondral bone in rotator cuff injuries.

In addition, we conducted a mechanical stress study on the collected rotator cuff samples to investigate the promoting effect of Cu/MnTA-HP on postoperative bone tendon interface regeneration (Figure 7F). As shown in Figure 7G,H, and Figure S23, the Cu/MnTA-HP group demonstrated higher maximum load and stiffness values compared to other groups at 2, 4, and 8 weeks. The CuTA-HP and MnTA-HP groups showed comparable maximum load and stiffness values. Furthermore, at the maximum load point, the Cu/MnTA-HP group showed improved performance compared to the control group. These results indicate that the tendon tissue in the Cu/MnTA-HP group healed well.

Moreover, a finite element model of the shoulder joint was reconstructed using CT scan data of the rat shoulder joint. Based on this model, we applied a tensile load of 200N to simulate the behavior of the tendon [44] (Figure S24). Under this 200N load, the stress levels at 8 weeks were 2668.5 MPa for the control group, 1627 MPa for the CuTA-HP group, 1790 MPa for the MnTA-HP group, and 1039 MPa for the Cu/Mn TA -HP group. These results indicated that the CuTA-HP and MnTA-HP groups exhibited a significant reduction in local stress levels compared to the control group. However, the Cu/MnTA-HP group demonstrated the lowest stress value, which was closer to the physiological stress value of 1000 MPa, suggesting that the Cu/MnTA-HP group had a more uniform distribution of stress at the tendon-bone interface, which reduces the risk of tendon rupture due to excessive localized stress.

2.9 | Transcriptomic Analysis Identifies PPARγ Signaling as a Key Pathway

To investigate the mechanisms by which Cu/MnTA-HP reduces fatty infiltration and promotes tendon regeneration, we performed transcriptomic analysis of supraspinatus tendon and muscle tissues at 8 weeks post-surgery (Figure S25A). Principal component analysis (PCA) revealed that the Cu/MnTA-HP group clustered closer to the Normal group than the Control group, indicating a reparative transcriptional landscape (Figure S25B). Differentially expressed gene (DEG) analysis identified 4326 genes between Normal and Control, and 4192 between Normal and Cu/MnTA-HP, with the treatment group showing substantial overlap with the Normal profile (Figure S25C,D). Gene Set Enrichment Analysis (GSEA) demonstrated that Cu/MnTA-HP treatment significantly enriched gene sets associated with "PPAR signaling pathway", "lipid storage", "response to fatty acid", and "regulation of lipolysis in adipocytes" compared to the Control group (Figure S25E–H). Consistently, GO enrichment analysis revealed downregulation of terms linked to "brown fat cell differentiation" and "lipid storage", alongside upregulation of "extracellular matrix organization" and "structural molecule activity" (Figure S26A–D). KEGG pathway analysis further converged on the PPAR signaling pathway and fatty acid biosynthesis as the top modulated categories (Figure S26E,F). These transcriptomic findings strongly suggest that Cu/MnTA-HP exerts its therapeutic effect primarily through inhibition of the PPARγ-driven adipogenic program.

2.10 | Proteomics Reveals the Specific Mechanisms of Microneedle Patches in Inhibiting Adipose Infiltration and Promoting Tendon-Bone Healing

To validate and extend the transcriptomic findings, we performed proteomic analysis on the same tissue samples (Figure 8A,B). Heatmap, boxplot, and PCA analyses consistently demonstrated that the Cu/MnTA-HP group exhibited a protein expression profile closer to the Normal group than the Control group (Figure 8C–E). Venn diagram analysis identified overlapping differentially expressed proteins among the three groups, suggesting that microneedle therapy may exert its effects by modulating specific protein sets (Figure 8F).

Differential protein expression analysis revealed that compared to the Control group, Cu/MnTA-HP treatment significantly

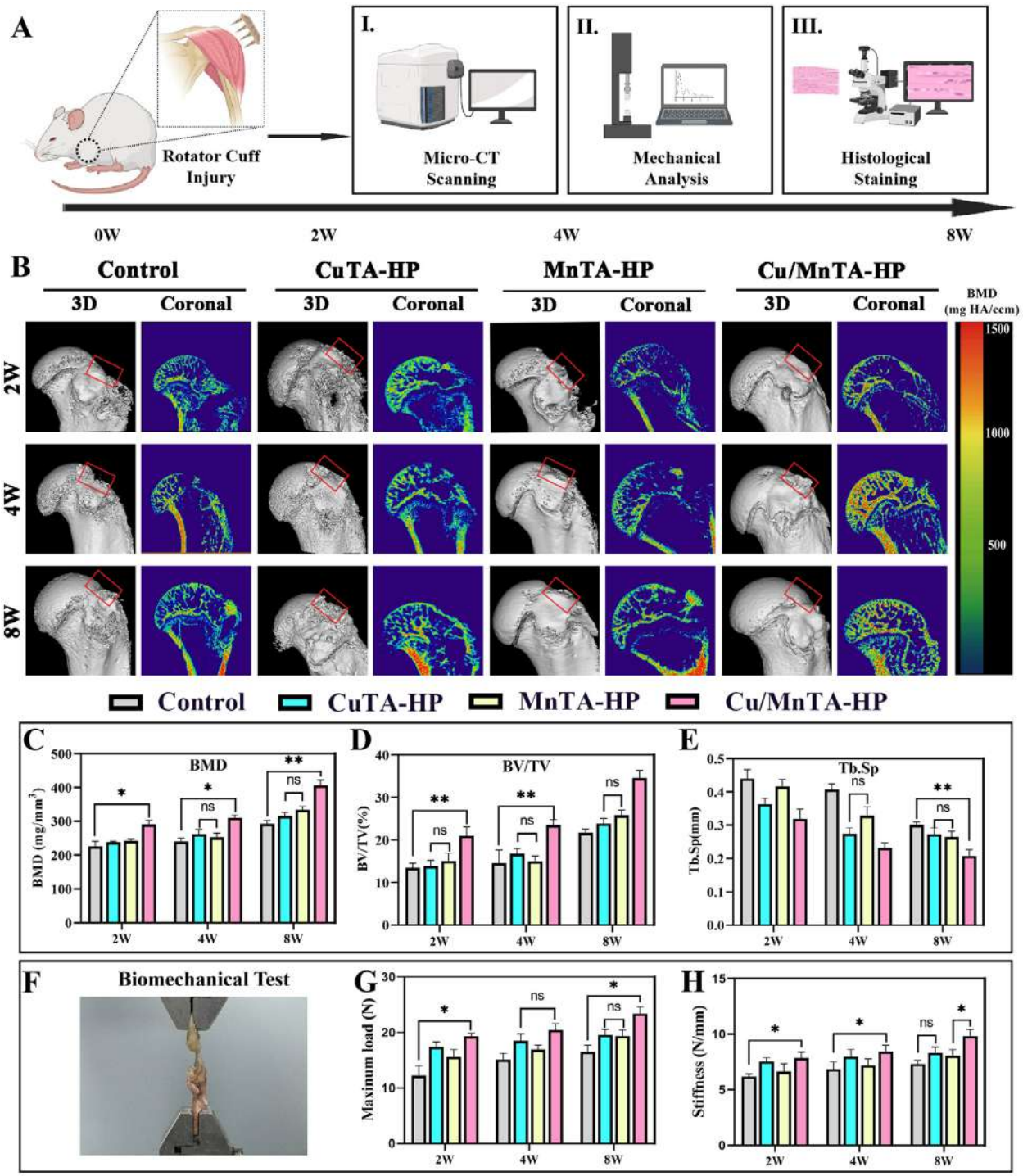

FIGURE 7 | Micro-CT analysis results and data for biomechanical tests of in vivo animal experiments. (A) Schematic of animal experiments. (B) Three-dimensional reconstruction images and coronal images of the proximal humerus micro-CT of rats at 4 and 8 weeks after surgery (n = 6). (C,D,E) BMD, BV/TV, and Tb.Sp values of the tendon-bone interface. (F) Images of biomechanical tests (n = 6). (G,H) Data for biomechanical tests, including maximum load and stiffness (n = 6). *$p < 0.05$, **$p < 0.01$, "ns" represents no significant difference.

downregulated lipid metabolism-related proteins including Cbr1l2, Scd1, and Abhd5, while upregulating Rbl2 and Lipe (Figure 8G–I). GSEA confirmed enrichment of pathways linked to mitochondrial function, muscle contraction, cytoskeleton in muscle cells, and regulation of lipolysis in adipocytes (Figure 8J). Consistently, Oil Red O staining showed markedly reduced fatty infiltration in the Cu/MnTA-HP group compared to the control (Figure 8K).

GO enrichment analysis indicated that Cu/MnTA-HP treatment downregulated terms associated with "fatty acid biosynthetic process" and "lipid droplet", while upregulating "structural

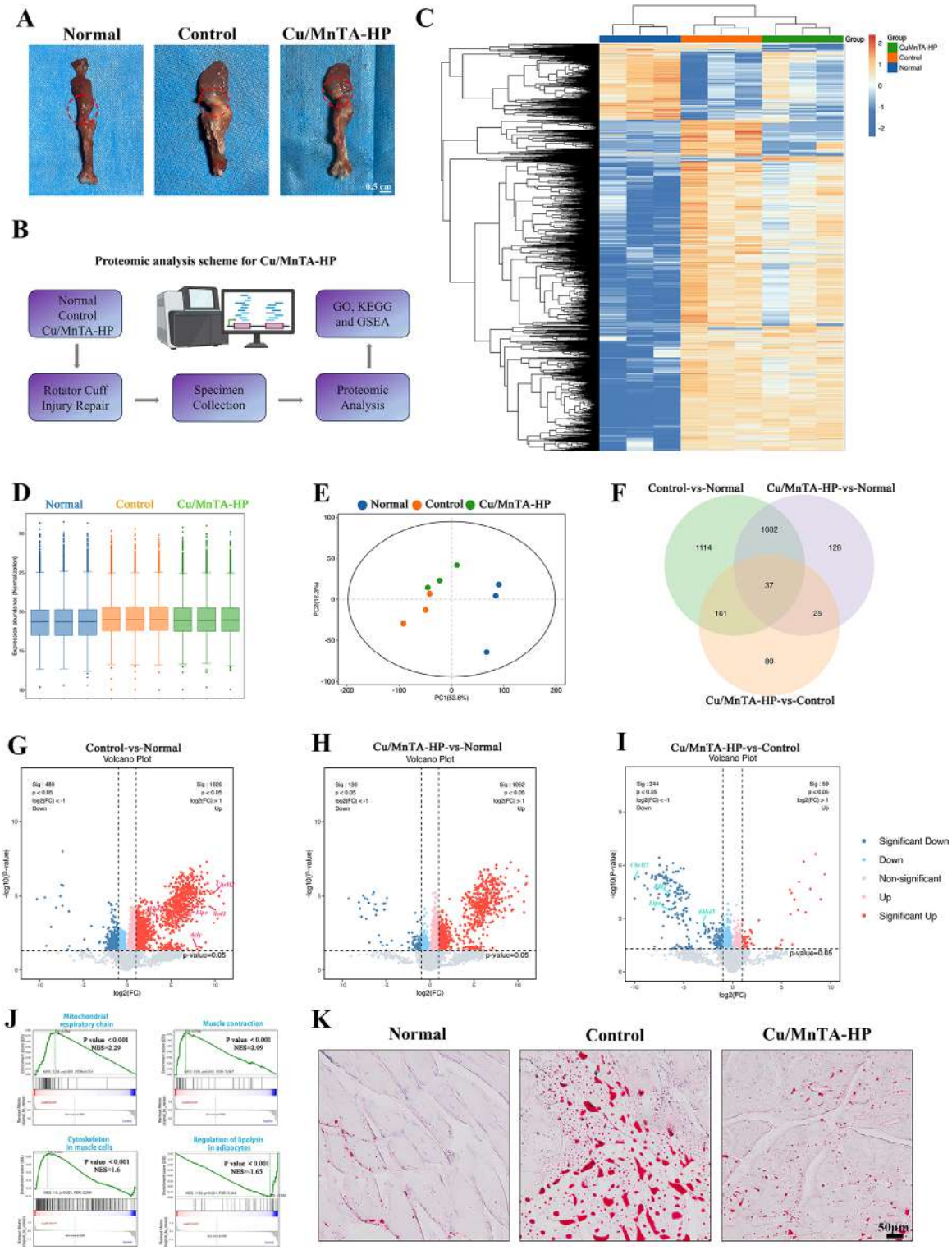

FIGURE 8 | Proteomic analysis of microneedle—promoted rotator cuff repair and reduced adipose infiltration. (A) Images of rat rotator cuff specimens from Normal, Control, and Cu/MnTA-HP groups (n = 3). (B) Proteomic sequencing protocol of microneedle patches. (C) Heatmap analysis of three groups. (D) Boxplot of proteomic data. (E) PCA. (F) Venn diagrams. (G—I) Volcano plots of protein expression in Control vs. Normal, Cu/MnTA—HP vs. Normal, and Cu/MnTA—HP vs. Control. (J) GSEA plots related to mitochondrial function, muscle contraction, cytoskeleton in muscle cells, and lipolysis regulation in adipocytes (Cu/MnTA—HP vs. Control). (K) Representative Oil Red O images of the rotator cuff muscle in three groups. Three samples were measured per group.

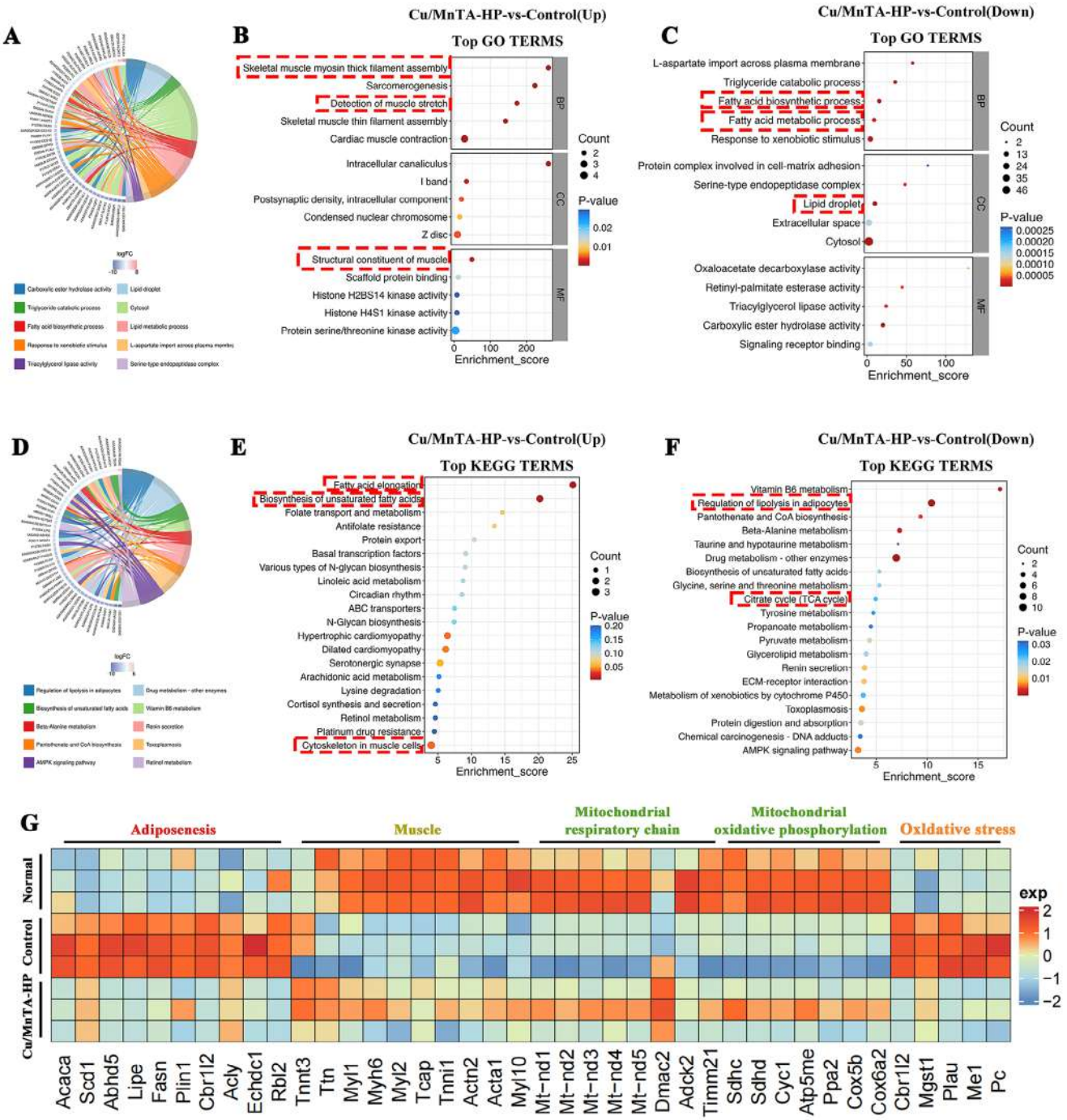

FIGURE 9 | Proteomics reveals the specific mechanism by which microneedle patches inhibit adipose infiltration and promote tendon bone healing. (A) Chord diagrams of GO enrichment for the Control group and Cu/MnTA-HP group. (B&C) The top 15 up-enrichment and top 15 down-enrichment of GO terms (Category: Molecular Function, Biological Process, and Cellular Component) in the Cu/MnTA-HP group compared to the Control group. (D) Chord diagrams of KEGG pathway enrichment for the Control group and Cu/MnTA-HP group. (E&F) The top 20 up-enrichment and top 20 down-enrichment of KEGG terms in the Cu/MnTA-HP group compared to the Control group. (G) Protein expression of Adiposenesis, Muscle, Mitochondrial function, and Oxidative stress -related proteins from proteomic profiles. All proteomic analyses used n = 3 biologically independent samples per group.

constituent of muscle" and "skeletal muscle myosin thick filament assembly" (Figure 9A–C). KEGG pathway analysis consistently pointed to the PPAR signaling pathway, fatty acid elongation, biosynthesis of unsaturated fatty acids, and regulation of lipolysis in adipocytes as the most significantly enriched categories (Figure 9D–F). Protein expression profiling further confirmed that Cu/MnTA-HP reduced adipogenic proteins (e.g., Plin1, Fabp4) and increased muscle- and mitochondrial-related proteins (Figure 9G).

Together, these proteomic results corroborate the transcriptomic findings and establish that PPARγ inhibition is a central mechanistic hub for the observed reduction in fatty infiltration and promotion of tendon-bone healing.

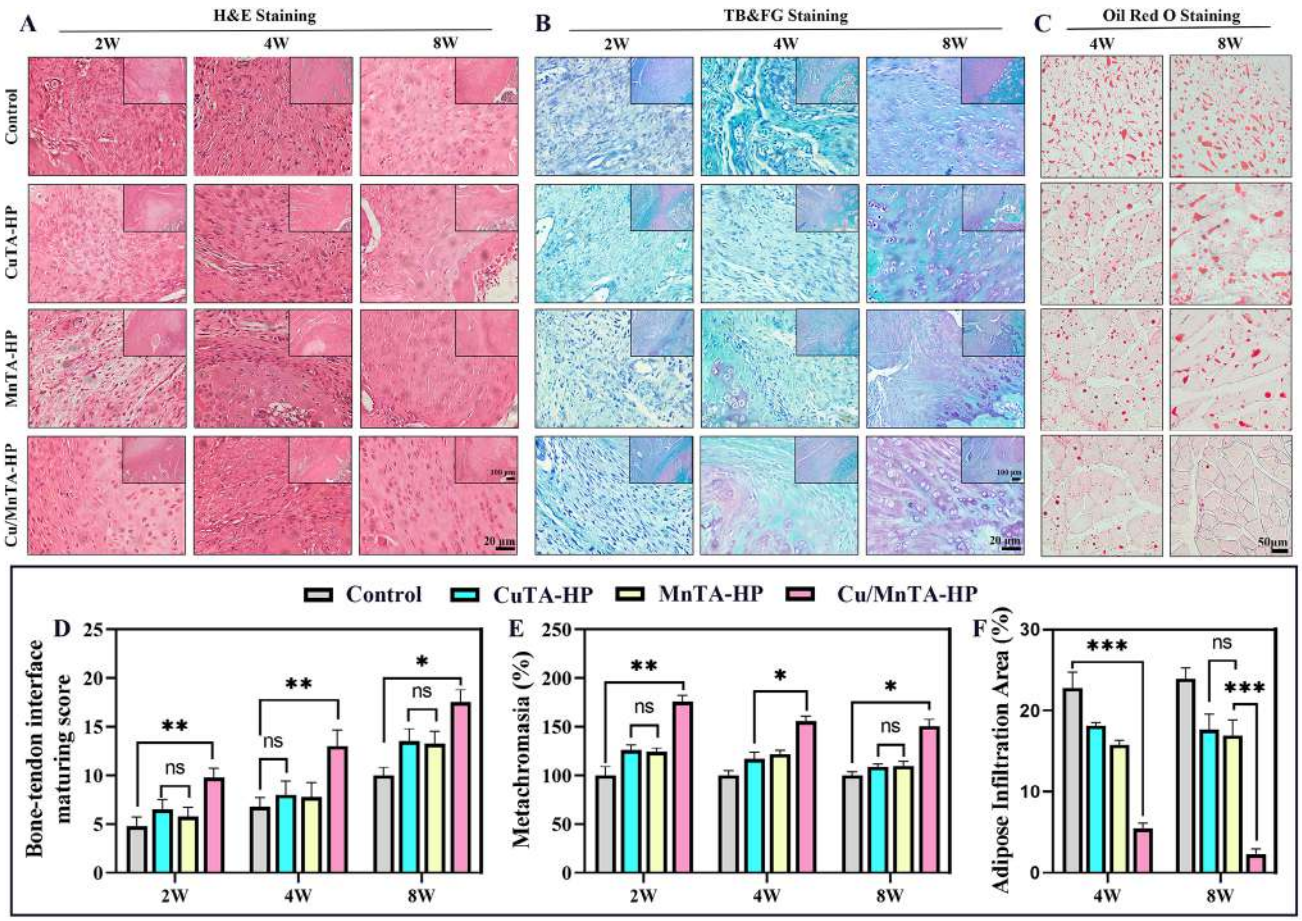

FIGURE 10 | Morphological analysis of newly formed tendon-bone interface tissues after treatment. (A) Representative images of hematoxylin and eosin (H&E)-stained sections (H&E)-stained and toluidine blue/fast green (B) of rat treated with suture, CuTA-HP, MnTA-HP, and Cu/MnTA-HP, respectively. T: tendon. I: Interface. B: Bone. (C) Representative oil red O images of rotator cuff muscle (n = 6). (D) Bone-tendon interface maturing score of different treatment groups (n = 6) and (E) the area of newly formed fibrocartilage in the different treatment groups (n = 6). (F) The adipose infiltration area of rotator cuff muscle in different treatment groups (n = 6). $^{*}p < 0.05$, $^{**}p < 0.01$, $^{***}p < 0.001$, "ns" represents no significant difference.

2.11 | Histological Analysis

To assess the microstructure of the repaired tissue, we performed H&E, toluidine blue, Oil Red O, Sirius red, and immunohistochemical staining at 2, 4, and 8 weeks postoperatively (Figure 10–12). At 2 weeks, all groups showed immature granulation tissue at the tendon-bone interface. By 4 and 8 weeks, the Cu/MnTA-HP group exhibited more organized collagen fibers and a larger fibrocartilage area compared to the Control, CuTA-HP, and MnTA-HP groups (Figure 10A,B). The interface maturing score was significantly higher in the Cu/MnTA-HP group at 8 weeks (Figure 10D) [45]. Toluidine blue staining revealed that fibrocartilage at the interface increased over time; at 8 weeks, the Cu/MnTA-HP group showed intact, well-organized tissue with normal cell morphology (Figure 10B,E).

Oil Red O staining of the supraspinatus muscle showed that fatty infiltration was significantly reduced in all microneedle-treated groups at 4 weeks. At 8 weeks, the Cu/MnTA-HP group exhibited markedly less fat accumulation ($2.19 \pm 0.59\%$) compared to the Control group ($24.28 \pm 1.35\%$, $p < 0.001$) (Figure 10C,F and Figure S27). In addition, the tissue sections were stained with Sirius red and observed under polarized light (Figure 11A–C). The oriented arrangement of collagen fibers at the tendon-bone interface is crucial for the integrity of its structure and function, which includes mechanical performance, uniform distribution of structure, gradient variation at the interface, and the stability of the tendon-bone junction. These results showed that at 2 weeks postoperatively, the collagen fibers in the four groups were not yet mature, and there was no significant difference in either the number or the fiber orientation (Figure 11D). In contrast, after 4 and 8 weeks, the direction of the collagen fibers in the Cu/MnTA-HP group was significantly more concentrated and orderly (Figure 11E). This suggests that the application of Cu/MnTA-HP contributes to the directional growth of collagen at the bone-tendon interface.

To elucidate the mechanism of Cu/MnTA-HP in tendon-bone interface repair, we performed immunohistochemical staining (Figure 12). The immunohistochemical results showed that the tendon-specific transcription factor SCX in the Cu/MnTA-HP group was significantly upregulated in the early stage of tendon repair, indicating enhanced initiation of tendon generation [46] (Figure 12A). As shown in Figure 12A,C, at 2 weeks, the expression of SCX was similar in the CuTA-HP group (94.4±17.1%) and the Control group. In contrast, SCX was significantly higher in the

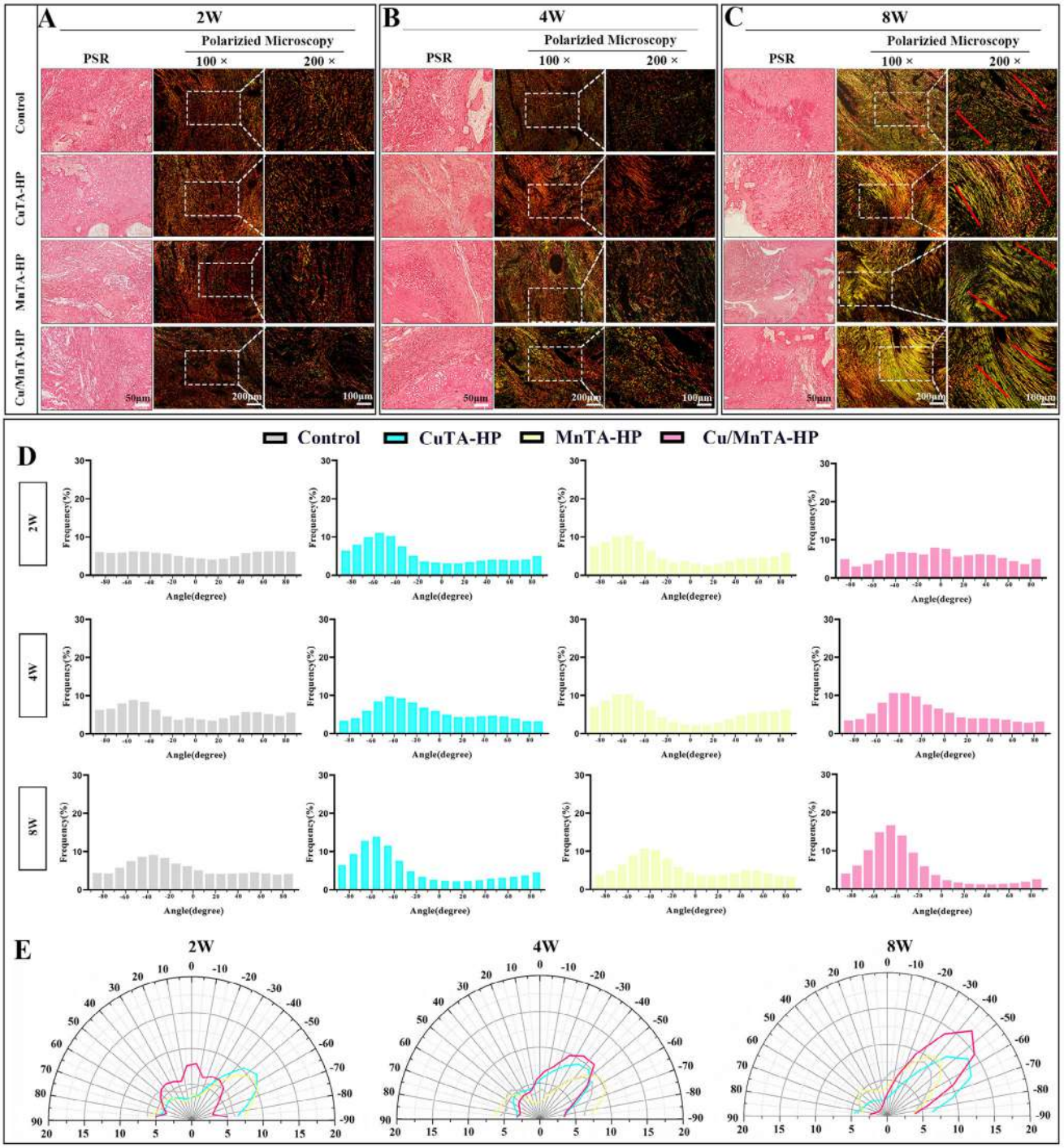

FIGURE 11 | Quantitative analysis of collagen fiber distribution at the bone tendon interface at 2, 4, and 8 weeks postoperatively. (A,B,C) Sirius red stained images of different treatment groups. (n = 6) (D) Distribution of collagen fiber orientation at 2, 4, and 8 weeks in different treatment groups. (E) Polar coordinates of collagen fiber orientation.

Cu/MnTA-HP group than in the other three groups (261.1±27.5%). At 4 and 8 weeks after surgery, although the Cu/MnTA-HP group showed higher levels of SCX expression, the difference was insignificant compared to the other groups at 2 weeks. We speculate that this may be due to the fact that SCX acts as a specific transcription factor for early tendon repair, and the Cu/MnTA-HP group has a more significant impact on the expression of SCX in the early stages of tendon regeneration. In the late stage of tendon repair, the delivery of Cu/MnTA nanozyme produced more mature tendon specific ECM, manifested as a significant upregulation of TNMD. Unlike SCX, TNMD showed significantly increased expression in the Cu/MnTA-HP groups at 4 and 8 weeks compared to other groups. This may be due to the protective effect of nanozymes on endogenous tendon cells (Figure 12B,D). These results collectively indicate that Cu/MnTA-HP can promote tendon regeneration and repair of the bone tendon interface by releasing biomimetic nanozymes and simulating enzyme activity in vivo.

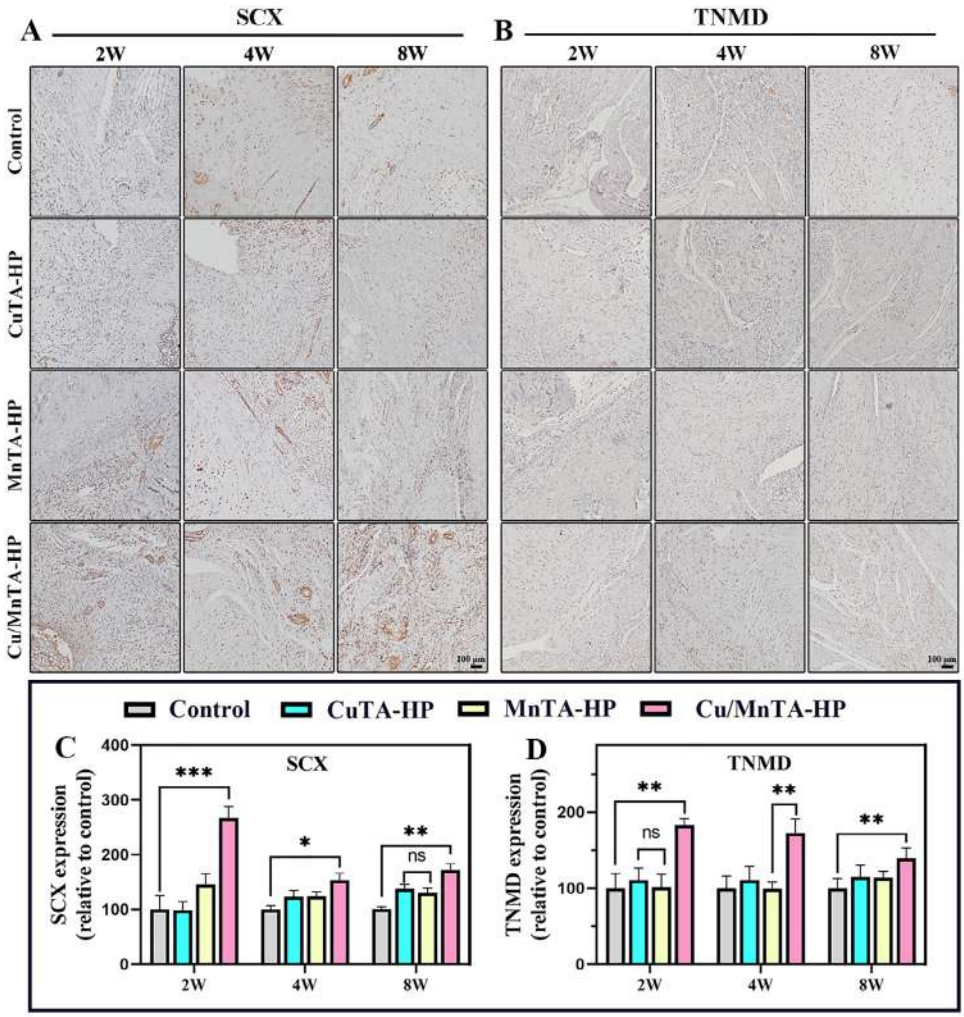

FIGURE 12 | Immunohistochemical staining of newly formed tendon-bone interface tissues after treatment. (A,B) Immunohistochemical staining images and associated expression levels (C,D) of SCX and TNMD at the tendon-bone interface in different treatment groups (n = 6) at 2, 4, and 8 weeks after treatment. $^{*}p < 0.05$, $^{**}p < 0.01$, $^{***}p < 0.001$, "ns" represent no significant difference.

Finally, correlation analysis was performed on the differentially expressed mRNAs and proteins. By employing bioinformatics methods to screen for common targets that exhibited significant changes at both transcriptional and translational levels, followed by pathway enrichment analysis, this integrated analysis clearly revealed that the PPAR signaling pathway is one of the most significantly regulated core pathways by Cu/MnTA-HP treatment. This suggests that the inhibition of the PPAR signaling pathway may be a key molecular event through which the microneedles exert their therapeutic effect. The regulation was visually confirmed at the spatial localization level through tissue immunofluorescence staining. In rotator cuff tissue sections at 8 weeks post-operation, both the fluorescence intensity of PPAR-γ-positive signal and the number of PPAR-γ-positive cells in Cu/MnTA-HP group were markedly lower than those in the Control group (Figure S28A), indicating effective inhibition of the activation and adipogenic differentiation. Concurrently, in the tendon-bone interface region, the positive expression of the tendon-specific transcription factor SCX was significantly enhanced and more widely distributed in the treatment group (Figure S28B), clearly demonstrating more active activation and differentiation of tenogenic cells during the repair process. Additionally, support was further provided at the gene transcription level by qPCR analysis. Detection of the same tissue samples showed that the mRNA expression of key adipogenic genes, PPAR-γ, CEBP-α, and FABP4, was synchronously and significantly downregulated in the Cu/MnTA-HP group (Figure S29). In concert with this, the transcription levels of tendon differentiation marker genes, SCX, TNMD, and Col I, were significantly upregulated (Figure S29). This collectively reveals, at the gene expression level, that the treatment effectively inhibits the adipogenic program while activating the tendon regeneration program.

3 | Discussion

This study emphasizes the critical role of tendon regeneration and the prevention of adipose accumulation in the healing process at the tendon-bone junction, an aspect often overlooked in previous rotator cuff injury repair. The development of an inflammatory-responsive microneedle patch laden with biomimetic SOD nanozymes (Cu/MnTA) presents a significant advancement. Upon ROS stimulation, the released mimetic

nanozymes enhance the differentiation of tendon-derived stem cells, curb local adipogenesis, and subsequently promote the repair of the tendon-bone interface. Crucially, our integrated transcriptomic and proteomic analysis, followed by multi-level validation, identified the inhibition of the PPARγ signaling pathway as a core molecular event underlying this dual therapeutic effect. Previous studies on rotator cuff injury repair have primarily focused on the regeneration of the tendon-bone interface, with little attention given to the impact of adipose infiltration in the surrounding muscles on the healing quality. Clinically, post-injury adipose infiltration in the rotator cuff has a more profound bearing on patient prognosis than the status of the tendon-bone interface repair, particularly in the elderly [47]. This study introduces innovative strategies aimed at enhancing the healing of the tendon-bone interface and mitigating adipose infiltration, thereby elevating the standard of improving healing outcomes.

Previous bioactive materials for tendon-bone interface repair have often focused on the interface itself, with little attention to the crucial role of mitochondrial function in tendon regeneration [48]. Additionally, an imbalance in the mitochondrial function of muscle cells can lead to lipid accumulation in the rotator cuff muscles [49]. SOD is an antioxidant metalloenzyme present in biological systems, which catalyzes the dismutation of superoxide anion radicals into oxygen and hydrogen peroxide, playing a vital role in the body's oxidation–antioxidation balance [50]. Therefore, we selected metal cofactors (Cu^{2+} and Mn^{2+}) consistent with natural SOD and combined them with TA to obtain mimetic SOD-like nanozymes (Cu/MnTA). Through NBT, DPPH, TMB, and OPD assays, we fully demonstrated that Cu/MnTA can simulate a series of natural enzymatic reactions (superoxide dismutase-like, peroxidase-like), helping to construct and maintain a favorable microenvironment. Importantly, by scavenging ROS and restoring mitochondrial bioenergetics, Cu/MnTA creates an intracellular milieu that suppresses the activation of the PPAR-γ pathway, a key regulator of adipogenesis. This mechanistic link explains the coordinated downregulation of adipogenic genes (e.g., PPAR-γ, CEBP-α, FABP4) and the concomitant upregulation of tenogenic markers (e.g., SCX, TNMD) observed in our qPCR and immunofluorescence analyses.

Using dynamic covalent boronate ester bonds between Cu/MnTA and phenylboronic acid-modified hyaluronic acid, we formed the polymer gel patch (Cu/MnTA-HP). Compared to hydrogels, the microneedle delivery system exhibits good fixation, ease of operation, and stable local drug administration, as confirmed by in vivo fluorescence tracing (Figure S14B). In clinical scenarios, rotator cuff repair is often challenged by local inflammatory reactions and adipose infiltration. Our microneedle platform, by enabling controlled release of Cu/MnTA under local ROS stimulation, shows promise in regulating the microenvironment and promoting tendon regeneration. However, the current results are limited to a rat model, and further studies are needed to evaluate its performance under clinically relevant conditions [13].

Mechanistically, we distinguished primary drivers from secondary effects. Using Rotenone (a mitochondrial complex I inhibitor), we showed that blocking mitochondrial function abolishes the therapeutic benefits, placing mitochondrial protection upstream of PPAR-γ inhibition. Using Rosiglitazone (a PPAR-γ agonist), we demonstrated that forced PPAR-γ activation reverses the anti-adipogenic and pro-tenogenic effects, proving that PPAR-γ downregulation is a mechanistic requirement, not an epiphenomenon. Furthermore, comparison with NAC revealed that Cu/MnTA-HP provides direct mitochondrial protection beyond ROS scavenging, possibly through metal ion-mediated stabilization of respiratory chain complexes. This refined model reconciles our multi-omics data with functional outcomes.

Histologically, Cu/MnTA-HP treatment significantly improved collagen fiber organization (Sirius red), increased fibrocartilage area (toluidine blue), reduced lipid droplet accumulation (Oil Red O), and enhanced tendon maturation scores compared to controls. Immunohistochemistry confirmed elevated SCX and TNMD expression at the healing interface (Figure 12) [38, 46]. Micro-CT showed greater bone volume fraction and trabecular density, and biomechanical testing revealed higher maximum load and stiffness (Figure 7). Collectively, these endpoints form a structure-function continuum, demonstrating functional regeneration rather than mere morphological improvement.

We acknowledge limitations. This study used a rat rotator cuff model with eight-week follow-up, which may not fully replicate human chronic tears or long-term remodeling. The direct mitochondrial target of Cu/MnTA remains to be identified (e.g., via copper-specific transporters or complex I binding). The potential systemic effects of released metal ions were not examined, although local application and the low dose (240 μg/mL) mitigate this concern. Future studies in large animal models with extended observation periods are needed before clinical translation.

In summary, the ROS-responsive Cu/MnTA-HP microneedle patch effectively promotes tendon-bone healing and reduces fatty infiltration in a rat rotator cuff model. The mechanistic cascade from ROS scavenging and mitochondrial protection to PPAR-γ inhibition and tenogenic fate switching provides a solid foundation for designing next-generation biomaterials for orthopedic repair.

4 | Conclusions

In summary, a simple one-step reaction method was employed to synthesize biomimetic nanozymes (CuTA, MnTA, or Cu/MnTA) in the presence of the natural polyphenol tannin acid (TA), by adding natural SOD metal cofactors such as Cu^{2+}, Mn^{2+}, or both Cu^{2+} and Mn^{2+}. These nanozymes were encapsulated within hyaluronic acid modified with phenylboronic acid to create ROS-responsive microneedle patches (CuTA-HP, MnTA-HP, or Cu/MnTA-HP) for the repair and prevention of adipose infiltration following rotator cuff injuries. The metal cofactors Cu^{2+} and Mn^{2+} coordinate with the pyrogallol groups of TA to form metal-polyphenol nanoparticles (Cu/MnTA), mimicking the structure and function of natural SOD enzymes. The NBT assay, DPPH assay, TMB assay, and OPD assay were used to demonstrate that Cu/MnTA can simulate and participate in a series of natural enzymatic reactions, exhibiting superoxide dismutase-like and peroxidase-like activities. This contributes

to the construction and maintenance of the microenvironment, as well as the preservation of cellular physiological states. The dynamic covalent boronate ester bond formed between Cu/MnTA and HP can dissociate naturally in a ROS-rich environment. Additionally, the released TA molecules, with their potent antioxidant capabilities, can scavenge endogenous ROS, thereby participating intelligently in the modulation of inflammatory responses, which is particularly beneficial for repairing the bone-tendon interface. Furthermore, Cu/MnTA-HP can effectively reverse the damage to the differentiation of tendon-derived stem cells caused by inflammatory environments, attributed to the nanozyme's functional improvement of mitochondria. In studies of fat accumulation, both in vivo and in vitro experiments have shown the superiority of Cu/MnTA-HP, supporting its promising application in bone-tendon interface repair and reduction of adipose deposition. This microneedle patch design strategy, which integrates the dual functions of promoting interfacial repair and preventing postoperative complications, may provide a useful platform for tendon-bone interface tissue engineering, though further studies in large animal models are warranted before clinical translation.

5 | Experimental Section

5.1 | Materials

Tanic acid (TA, Mw = 1701.2 Da), copper chloride ($CuCl_2$, Mw = 134.45 Da), manganese chloride tetrahydrate ($MnCl_2{\cdot}4H_2O$, Mw = 197.9 Da), and 3-Aminophenylboronic acid hydrochloride (PBA) were purchased from Macklin Reagent. 1-(3-Dimethylaminopropyl)-3-ethylcarbodiimide (EDC), N-Hydroxy succinimide (NHS), and hyaluronic acid (HA) were purchased from Sigma-Aldrich. All chemicals were used without further purification. Polydimethylsiloxane (PDMS) molds were purchased from Taizhou Microchip Pharmaceutical Technology Co., Ltd. (Taizhou, China).

5.2 | Synthesis of CuTA, MnTA and Cu/MnTA Nanozymes

Tannic acid (TA) was used to modify $CuCl_2/MnCl_2$ (CuTA/MnTA) via a one-step method. Based on previous studies, the appropriate ratio of metals and polyphenols for the reaction was determined [27, 51]. Put 2.5 g TA and 30 mL sterile water to the centrifuge tube with a capacity of 50 mL to synthesize CuTA nanozymes. After mixing the solution thoroughly under neutral conditions, gradually adjust the pH to alkaline (10-12). Additionally, add 2.5 g copper chloride to the centrifuge tube (Figure S1). After mixing the reaction thoroughly, the crude product was collected by centrifugation at 8000 rpm for 5 min. Further purification was achieved by washing the product with sterile water for at least three cycles. Finally, the purified CuTA nanozymes were obtained by freeze-drying. MnTA nanozymes were also synthesized through the above methods and steps. Cu/MnTA nanozymes were synthesized by uniformly mixing 2.5 g TA with 30 mL sterile water and adding 1.25 g $CuCl_2$ and 1.25 g $MnCl_2$. Mix evenly under alkaline conditions and use the above centrifugation and collection methods to obtain Cu/MnTA nanozymes.

5.3 | Characterization of CuTA, MnTA and Cu/MnTA Nanozymes

Scanning electron microscopy (SEM) images and energy dispersion (EDS) data of CuTA, MnTA, and Cu/MnTA nanozymes were obtained using a Zeiss Sigma 300 microscope (Germany), and the particle size analysis was also conducted by measuring the sizes of at least 250 particles and averaged. Fourier transform infrared spectra (FTIR) were recorded using a Thermo Scientific Nicolet-iS10 FTIR spectrometer. The crystallinity and elemental composition of CuTA, MnTA, and Cu/MnTA nanozymes were characterized by X-ray diffraction (XRD, Bruker D8) and X-ray photoelectron spectroscopy (XPS, Thermo Fisher Scientific, Escalab 250Xi). Thermogravimetric analysis (TGA) was performed using a thermogravimetric analyzer (NETZSCH STA 449F3) from Neuilly, Germany, under N2 atmosphere at a heating rate of 10°C per minute.

5.4 | Synthesis and Characterization of Phenylboronic Acid Modified Hyaluronic Acid Polymer (HP)

HA (200 mg, 0.54 mmol), 0.04 g of EDC (Macklin), and 0.04 g of NHS (Macklin) were completed dissolved in a mixture of 4 mL DMF and 6 mL H_2O, and PBA (125 mg, 0.65 mmol) was added, followed by tuning the pH of the solution to 6.5. The solution mixture was stirred at room temperature for 48 h and transferred to a dialysis bag (3000 g/mol cutoff). After three days of exhaustive dialysis against DI water, the solution was lyophilized to obtain the HP. The HP polymers were characterized by FTIR Spectrometer (Thermo Scientific Nicolet-iS10) and ^1H NMR (D^2O was selected as solvent, AVANCE NEO 400, Bruker).

5.5 | Fabrication and Characterization of CuTA-HP,MnTA-HP and Cu/MnTA-HP

Dissolve CuTA at 240 μg/mL in the prepared HP solution. DMNs were prepared using PDMS molds. Briefly, the master mold consisted of a 0.8 × 0.8 cm base and 225 (15 × 15) quadrilateral pyramid-shaped microneedles. Add 400 μL of the tip solution to the PDMS mold, centrifuge to fill the cavity, remove the remaining solution, and solidify the tip for 30 s. Add 300 μL of the bottom solution to completely cover the tip of the mold, centrifuge to remove bubbles, dry at constant temperature (25°C) and constant humidity (5%) for 72 h, demold, and recover DMN to obtain CuTA-HP microneedle. MnTA-HP microneedle and Cu/MnTA microneedle were obtained through the same procedure. A blank microneedle (blank DMN, HP without drug) was obtained through the same procedure to serve as a control.

An FTIR Spectrometer (Thermo Scientific Nicolet-iS10) was used to test HA powder, HP, CuTA-HP, MnTA-HP, and Cu/MnTA-HP lyophilized sample. ^1H NMR analysis was measured using a fourier 80 spectrometer (AVANCE NEO 400, Bruker). Scanning electron microscopy (SEM) images and energy dispersion (EDS) data of CuTA-HP, MnTA-HP, and Cu/MnTA-HP were obtained using a Zeiss Sigma 300 microscope (Germany). The mechanical properties of microneedles were determined by an Instron 34TM-10 testing machine. When the upper plate initially contacts the

microneedle tip, the distance between the upper and lower plates is zero. The lower plate moves upward to MN at a constant speed of 0.1 mm/min until the needle bends and breaks. Record the compression curve of each microneedle. The H_2O_2-sensitive test was conducted by adding a MN in a PBS solution (pH 7.4) with 0, 0.2, 0.5, and 1 mM H_2O_2, which was placed in a 37°C shaker. At predetermined time intervals (0, 24, 48, and 96 h), the MNs in different solutions were captured and recorded. The concentration of TA in the release medium was determined using a UV/Vis spectrophotometer (Shimadzu 2600i, Japan) at 276 nm. Three parallel measurements were taken for each sample, and the results were averaged to obtain more accurate data.

5.6 | Experiments of Enzyme-Like Activity

5.6.1 | SOD-Like Activity Determination

A commercially available superoxide dismutase detection kit (S0109, Beyotime) was used to detect the SOD-like activity of these nanozymes. Briefly, NBT is a probe for detecting superoxide anions and is used to evaluate the $O_2^{\bullet-}$ scavenging activity of nanozymes. Different concentrations of nanozymes and NBT were mixed with riboflavin and methionine in PBS buffer, and record the absorbance at 550 nm.

5.6.2 | Superoxide Anion Scavenging Activity Evaluated by EPR Spectroscopy

The superoxide anion ($\bullet O_2^-$) scavenging capacities of tannic acid (TA) and the Cu/MnTA nanozyme were quantitatively assessed using electron paramagnetic resonance (EPR) spectroscopy with DMPO as the spin trap. The characteristic six-line EPR signal of the DMPO/$\bullet O_2^-$ adduct was clearly detected in the control system containing the $\bullet O_2^-$ source.

5.6.3 | DPPH Radical Scavenging Assay

The antioxidant activity of nanozymes (CuTA, MnTA, and Cu/MnTA) was evaluated using the DPPH radical scavenging method. 3 mg sample was added to a 3.0 mL ethanol solution of DPPH (100 μmol/L). The mixture was incubated in darkness for 3 min. Subsequently, a wavelength scan was performed using a UV-vis spectrophotometer (Shimadzu 2600i, Japan). The degradation rate of DPPH was determined using Equation (1), where AB represents the absorbance of the blank (DPPH + ethanol), and AS represents the absorbance of the sample (DPPH + ethanol + sample).

$$\text{DPPH clearance rate } (\%) = \frac{A_B - A_s}{A_B} \times 100 \quad (1)$$

5.6.4 | The Peroxidase-Like Property of Nanozymes (TMB and OPD Assays)

The antioxidant activity of nanozymes is detected based on the catalytic oxidation of 3,3′,5,5′-tetramethylbenzidine (ST746, Beyotime), which produces the creation of a characteristic blue product. Briefly, the nanozymes were mixed with a mixture consisting of 20 μL of 0.5 M H_2O_2 buffer (pH 4.0) and 10 μL of 16 mM TMB solution. The resulting mixture was incubated at different time intervals and detected by UV-visible absorption spectroscopy at 650 nm. In addition, OPD was also adopted to characterize the peroxidase-like activity of TCNH with a similar method as TMB for the UV–vis absorbance of the product 2,3-diaminophenazine (DAP) at 432 nm.

5.7 | In Vitro Cell Experiments

5.7.1 | Isolation and Culture of TDSCs

Male Sprague-Dawley rats (4 weeks old) were sacrificed by cervical dislocation. TDSCs were isolated from rat Achilles tendons. Under sterile conditions, cut the tendon evenly into 1mm×1 mm size and digest it with type I collagenase for 1 h. The resulting cells, including undigested tendon tissue, were then seeded in Alpha-modified Eagle's medium (αMEM) supplemented with 10% FBS and 1 × penicillin-streptomycin. After 48 h, non-adherent cells were removed. When the cells reach 100% confluence, perform subculture and increase the culture passage to passage 1 (P1). The cells were passed to Passage 3 (P3) for subsequent experiments.

5.7.2 | Biocompatibility of Nanozymes In Vitro

To detect the toxicity of the nanozymes, the basal medium was used to dilute it into gradient concentrations (30, 60, 120, 240, 500, 1000, 2000, 4000, and 8000 μg/mL). Then, disinfect with UV light and alcohol for 12 h. Cytotoxicity assay was performed using Cell Counting Kit-8 (CCK-8, Servicebio, China). The viability of TDSCs was evaluated after co-culture with nanozyme at 24, 48, and 72 h respectively. For cells treated with the different concentrations of nanozymes, a Live/Dead Viability/Cytotoxicity Kit (L32250, Thermo Fisher Scientific) was used to stain the cells. The morphology of the cells was observed using an inverted fluorescence microscope (Leica DMI4000 B, Leica Microsystems GmbH, Wetzlar, Germany).

5.7.3 | Cell Migration Assays

Scratch and transwell assays allow assessment of cell migration responses to nanozymes. TDSCs were seeded in 6-well plates at a cell density of 3×10^4 cells/well. Cells were cultured in complete αMEM for 24 h to form a cell monolayer. Use a 200 μL pipette tip to make three parallel scratches in the cell monolayer. The floating cells were washed three times with sterile PBS (pH 7.4) to remove non-adherent cells. The remaining cells were incubated for another day in a complete αMEM containing nanozymes. After 6, 12, and 24 h, cells were observed and photographed using an inverted microscope (Olympus CKX41, Tokyo, Japan). Based on Equation (2), use Image J or analysis software to calculate the cell migration rate quantitatively.

$$\text{Migration rate } (\%) = \frac{W_i - W_t}{W_i} \times 100 \quad (2)$$

Here, Wi represents the initial scratch width at 0 h, and Wt represents the scratch width after t hours of culture (t = 8 or 24).

Transwell assays were performed using a transwell chamber (Corning, 353097) placed within a 24-well plate containing αMEM wells. TDSCs were seeded in 100× degradation products (500 μL/chamber) at a density of 3×10^4 cells/mL and incubated for 6, 12 and 24 h. After incubation, wipe gently with a cotton swab to completely remove cells from the upper surface of the chamber. Subsequently, cells on the lower surface were fixed using a 5% glutaraldehyde solution for 30 min and stained with crystal violet, an alkaline dye that binds to DNA in the cell nucleus, thereby providing nuclear staining. The chamber was washed with sterile PBS before observation and photography using a microscope (Olympus CKX41, Tokyo, Japan).

5.7.4 | ROS Determination Test

A ROS assay assessed the intracellular ROS scavenging ability of nanozymes and nanozymes -loaded microneedles. TDSCs were inoculated in the wells of a 24-well plate and incubated at 37°C for 12 h to allow cell attachment and growth. The cells were then incubated with nanozymes or microneedles for 24 h. Cells were subsequently incubated with DCFH-DA assay reagent (diluted at a ratio of 1:1000) for 20 to 30 min to enable visualization of intracellular ROS in 24-well plates using an inverted fluorescence microscope (Leica DMI4000 B). The ROS assay allowed for evaluation and observation under fluorescence microscopy, which provided insight into the potential antioxidant properties.

5.7.5 | Oil Red O Staining and Cell Immunofluorescence of PPAR-γ

3T3-L1 cells were used to assess adipogenic differentiation, as previously described [41]. 3T3-L1 cells were seeded at a density of 2×10^4 cells in a 24-well plate. Different microneedles were used to pretreat lipid culture media in the experiment. Change the culture medium every 48 h. After 7 days of cultivation induction, 3T3-L1 cells were subjected to immunofluorescent and oil red O staining (Solarbio, China).

5.7.6 | Cell Immunofluorescence of Tendon-Specific Markers Under Oxidative Stress Model

To simulate the oxidative stress microenvironment, TDSCs were exposed to 1×10^{-4} M H_2O_2 (Sigma–Aldrich, USA) in serum-free α-MEM for 4 h. Then, the complete culture medium of α-MEM soaked with different microneedles was refreshed, cultured for 3 days, washed twice with PBS, and TDSCs were fixed with 4% PFA. After blocking with 1% BSA (Servicebio, China), the samples were incubated in primary antibodies (Abmart, China), anti-SCX (1:200), anti-TNMD (1:200), and anti-Col I (1:200) at 4°C overnight. The following day, secondary antibodies (Abcam, USA) were added following three rinses and incubated at 37°C for 2 h. The secondary antibodies were washed away, and the cell nuclei were stained with DAPI (Beyotime, China) for 5 min. The immunofluorescent cells were then observed and photographed under an inverted fluorescence microscope.

5.7.7 | Validation of Microneedle Promoted Osteogenesis

To summarize, TDSCs were seeded onto coverslips and cultured with osteogenic induction medium soaked with different microneedles, with the medium being changed every two days. After 7 days of culture in osteogenic medium, cells were fixed with 4% PFA, blocked with 1% BSA (Servicebio, China), and incubated overnight at 4°C with anti-RUNX2 (1:200) and anti-ALP (1:200) antibodies. On the following day, after three washes, secondary antibodies and cytoskeleton staining (Phalloidin) were applied and incubated at 37°C for 2 h. Afterward, the secondary antibodies were washed off, and the nuclei were stained with DAPI (Beyotime, China) for 5 min. Immunofluorescent cells were subsequently observed and imaged under an inverted fluorescence microscope.

5.7.8 | Detection of ATP Level, ROS Level, Mitochondria Membrane Potential, and ATP Production

Cellular ATP levels were measured photometrically using an ATP assay reagent (Beyotime, China) according to the instructions. TDSCs lysates were collected and used to determine ATP content. At the same time, the ROS detection kit (Beyotime, China) and MitoSox mitochondrial superoxide indicator (Thermo Scientific, USA) were used to detect ROS and superoxide of TDSCs [42]. JC-1 (Beyotime, China) was used to detect the mitochondrial membrane potential of TDSCs. Briefly, after TDSCs were exposed to 0.5 mM H_2O_2 in serum-free MEM for 6 h, the probes were mixed with serum-free medium and diluted to working concentrations. After incubation for 30 min, the cell nuclei were stained with DAPI (Beyotime, China) for 5 min. The immunofluorescent cells were observed and imaged using an inverted fluorescence microscope. Mitochondrial morphology was examined by transmission electron microscopy (TEM). Briefly, TDSCs from each group were fixed, dehydrated, embedded, and sectioned, followed by uranyl acetate and lead citrate staining. Images were acquired using a Thermo Fisher TEM.

5.7.9 | Gene Expression Analysis

Quantitative PCR was applied to detect the expression of specific genes. Total RNA was isolated using a Trizol reagent (Invitrogen, USA). 1000 ng RNA was reverse transcripted using the First Strand cDNA Synthesis Kit (Thermo fisher, USA). SYBR green PCR Master Mix (Thermo fisher, USA) was used in qPCR with CFX96 Connect Real-Time PCR Detection System (BIO-RAD, USA). ΔΔCt method was applied to calculate the results. The primers used in this study were designed by Primer 3.0 (Table S1).

5.8 | Animal Studies

5.8.1 | Surgical Procedures

All animal experiments were performed according to the Institute of Biological and Medical Engineering, Guangdong Academy of Sciences (Approval K-2023-01-157). Briefly, 144 8-week-old male

SD rats were purchased from the Medical Animal Experiment Center of Southern Medical University. They were randomly divided into 4 groups: Control group, CuTA-HP group, MnTA-HP group, and Cu/MnTA-HP group, with 36 animals in each group. The rotator cuff tear model was created using established methods [31]. After administration of anesthesia, the rats were placed in the lateral decubitus position. A longitudinal incision is made in the anterolateral portion of the shoulder to expose the supraspinatus tendon. The deltoid muscle is also divided to allow better visualization of the tendon. The tendon is then separated at its insertion into the greater tuberosity of the humerus. Use a #7 angle needle to drill a tunnel through the key prominence of the humerus. After removing any residue from the footprint, the retracted tendon is pulled through the bony groove. Use 5# sutures to suture the supraspinatus muscle back to the greater tubercle. The nanozymes-loaded microneedle is then pressed and allowed to penetrate the muscle belly proximal to the insertion of the supraspinatus tendon. The Control group did not use microneedle treatment. Finally, the wound was sutured, and the rats had free access to water and food in the cages. Antibiotics (penicillin, 100 000 units of intramuscular injection per day) were used for 3 days after surgery to prevent postoperative infections.

5.8.2 | Micro-CT Analysis, Finite Element Analysis and Biomechanical Testing

At weeks 2,4 and 8 post-operation, SD rats were euthanized, and the bone-tendon interface specimens (6 for micro-CT and histology study,6 for biomechanical testing) were fixed in 4% paraformaldehyde and stored at 4°C.

Micro-CT (Viva CT40, Switzerland) was conducted in an isolated bone mode to evaluate the bone regeneration in the defect area. The coronal image of the bone-tendon interface sections was reconstructed using Mimics software (version 20.0). A cylindrical space representing the volume of interest (VOI) was designated to evaluate new bone formation by calculating BMD, bone volume fraction (BV/TV), number of bone trabeculae (Tb. N), thickness of bone trabeculae (Tb. Th), separation of bone trabeculae (Tb. Sp) using Latheta software (Scanco Medical AG, Bassersdorf, Switzerland).

The finite element model was constructed using Ansys 19.0 software, on which the material properties of each part of the 3D model structure were defined [30]. The material properties of the cortical bone of the humeral head are 1.5×10^4 MPa, and the material properties of the supraspinatus tendon are 10 MPa. Simulates the tension of the supraspinatus tendon (200N) and outputs stress-strain data at the same time.

The supraspinatus tendon-humerus complexes from each group (n = 6) were harvested 2 weeks, 4 weeks, and 8 weeks after RCR surgery. Testing was performed using an electronic general material testing system (Instron 5569). Briefly, the samples were preconditioned with 0.1 N and then loaded to failure under uniaxial tension at an elongation rate of 10 mm/min. The failure load was recorded, and the stiffness was calculated from the load-deformation curve.

5.8.3 | RNA Sequencing and Analysis

At postoperative week 8, tissues attached to the supraspinatus tendon and muscle belly where microneedles had been implanted, were collected for A total of nine sample libraries (three each for the Normal, Control, and Cu/MnTA-HP groups) were constructed by OE Biotech Co., Ltd. (Shanghai, China) using the NEBNext Ultra II RNA Library Prep Kit and subsequently sequenced on an Illumina NovaSeq PE150 platform. The reference genome index was built, and raw gene expression levels were quantified using HTSeq (v0.9.1), with expression values normalized by FPKM. Differential expression analysis was performed using DESeq (v1.38.3). For biological function interpretation, GO term and KEGG pathway enrichment analyses were conducted sequentially, followed by Gene Set Enrichment Analysis (GSEA) to identify potential regulatory mechanisms.

5.8.4 | Proteomic Analysis

At postoperative week 8, tissues attached to the supraspinatus tendon and muscle belly, where microneedles had been implanted, were collected for proteomic analysis (performed by OE Biotech Co., Ltd.). Nine sample libraries (three each for the Normal, Control, and Cu/MnTA-HP groups) were prepared as previously described. For proteomic data analysis, a suite of tools was employed, including DAVID, STRING, Cytoscape, CytoHubba, and OmicStudio. Proteins with a p-value below 0.05 were identified as differentially expressed proteins (DEPs) and were subjected to subsequent co-enrichment analysis to further elucidate their functional roles and interactions.

5.8.5 | Histological Analysis, Immunohistochemical Staining, Immunofluorescence Staining and Gene Expression Analysis

The supraspinatus tendon-humeral complexes were removed at 2,4 and 8 weeks postoperatively, scanned by micro-CT, fixed with 4% paraformaldehyde, and decalcified with 0.5 M EDTA at 37°C for 4 weeks. After dehydration and embedding in paraffin, the samples were cut into 4-mm-thick sections. Additionally, we removed the supraspinatus tendon muscle belly, fixed and sliced it. These samples were stained with hematoxylin and eosin (H&E), toluidine blue (TB), oil red O, and picrosirius red (PSR). light microscope (IX71SBF-2, Olympus) examined the H&E, TB, and oil red O-stained slides. The metachromasia area in the TB-stained slides was measured using the Image J software. Polarized light microscopy (Eclipse E800, Nikon) was used to examine the collagenous organization of tendons near the greater tuberosity in bitter almond red slides [43]. Fiber orientation was counted using Image J. The histologic scoring system is used to assess the interface between tendon and bone semi-quantitatively.

Immunohistochemical staining for SCX and TNMD was performed and observed with an orthogonal fluorescence microscope (Leica DMI4000B). Semi-quantitative analysis of SCX and TNMD positively stained cells was performed using Image J.

Immunofluorescence staining for PPAR-γ and SCX was performed on paraffin-embedded tissue sections and observed with a fluorescence microscope. Total RNA was extracted from rotator cuff tissues, reverse transcribed into cDNA and subjected to quantitative real-time PCR (qPCR) using gene-specific primers. The relative mRNA expression levels were calculated using the 2−ΔΔCt method with normalization to GAPDH.

5.8.6 | Statistical Analysis

For in vitro experiments, data are presented as mean ± SD from at least three independent biological replicates (n = 3 or 4). For in vivo experiments, data are presented as mean ± SD from six biologically independent animals per group per time point (n = 6). Statistical comparisons between two groups were performed using two-tailed unpaired Student's t-test. For multiple group comparisons, one-way or two-way analysis of variance (ANOVA) was used, followed by Tukey's or Bonferroni's post-hoc test as appropriate. A value of $p < 0.05$ was considered a statistically significant difference. *, ** and *** represent $p < 0.05$, $p < 0.01$ and $p < 0.001$, respectively. All statistical analyses were performed using GraphPad Prism 10 (GraphPad Software, San Diego, CA, USA).

Acknowledgements

Funding: This work was supported by the National Students' Platform for Innovation and Entrepreneurship Training Program of China (Grant Number. 202312121005), the Youth Talent of Guangdong Special Support Program (0620220207), the Guangdong Basic and Applied Basic Research Foundation (Nos. 2022A1515011101 and 2024A1515012664), the Natural Science Foundation of Guangdong Province (No. 2024A1515011231), the Science and Technology Plan Program of Guangzhou (No. 2023A04J2461) and the Clinical Research Special Fund of the president 's Foundation of the Third Affiliated Hospital of Southern Medical University (No. YL202206).

Conflicts of Interest

The authors declare no conflicts of interest.

Data Availability Statement

The data that support the findings of this study are available from the corresponding author upon reasonable request.

References

1. A. Bedi, J. Bishop, J. Keener, et al., "Rotator Cuff Tears," *Nature Reviews Disease Primers* 10 (2024): 8, https://doi.org/10.1038/s41572-024-00492-3.

2. J. S. Lewis, "Rotator Cuff Tendinopathy," *British Journal of Sports Medicine* 43 (2009): 236–241, https://doi.org/10.1136/bjsm.2008.052175.

3. A. Yamamoto, K. Takagishi, T. Osawa, et al., "Prevalence and Risk Factors of a Rotator Cuff Tear in the General Population," *Journal of Shoulder and Elbow Surgery* 19 (2010): 116–120, https://doi.org/10.1016/j.jse.2009.04.006.

4. J. S. Sher, J. W. Uribe, A. Posada, et al., "Abnormal Findings on Magnetic Resonance Images of Asymptomatic Shoulders," *The Journal of Bone and Joint Surgery American Volume* 77 (1995): 10–15.

5. R. Buchbinder, S. Green, J. M. Youd, R. V. Johnston, and M. Cumpston, "Arthrographic Distension for Adhesive Capsulitis (frozen shoulder)," *Cochrane Database of Systematic Reviews* 2010 (2008): CD007005, https://doi.org/10.1002/14651858.CD007005.

6. A. Mohamadi, J. J. Chan, F. M. A. P. Claessen, D. Ring, and N. C. Chen, "Corticosteroid Injections Give Small and Transient Pain Relief in Rotator Cuff Tendinosis: a Meta-analysis," *Clinical Orthopaedics & Related Research* 475 (2017): 232–243, https://doi.org/10.1007/s11999-016-5002-1.

7. A. Jaggi and S. Lambert, "Rehabilitation for Shoulder Instability," *British Journal of Sports Medicine* 44 (2010): 333–340, https://doi.org/10.1136/bjsm.2009.059311.

8. L. Gebremariam, E. M. Hay, R. van der Sande, W. D. Rinkel, B. W. Koes, and B. M. A. Huisstede, "Subacromial Impingement Syndrome—Effectiveness of Physiotherapy and Manual Therapy," *British Journal of Sports Medicine* 48 (2014): 1202–1208, https://doi.org/10.1136/bjsports-2012-091802.

9. H. Jin, Z. Deng, J. Sun, D. T. A. Vithran, W. Xiao, and Y. Li, "Surgical Management for Massive Rotator Cuff Tears: a Network Meta-analysis of Randomized Controlled Trials," *Burns & Trauma* 12 (2024): tkad052, https://doi.org/10.1093/burnst/tkad052.

10. Y. Itoigawa, H. Uehara, H. Tsurukami, et al., "The Combined Suture Bridge with Mason-Allen Technique Is Superior to the Conventional Suture Bridge Technique for Arthroscopic Rotator Cuff Repair," *Arthroscopy* 40 (2024): 674–680, https://doi.org/10.1016/j.arthro.2023.07.009.

11. M. S. Rashid, C. Cooper, J. Cook, et al., "Increasing Age and Tear Size Reduce Rotator Cuff Repair Healing Rate at 1 Year," *Acta Orthopaedica* 88 (2017): 606–611, https://doi.org/10.1080/17453674.2017.1370844.

12. J. J. Barry, D. A. Lansdown, S. Cheung, B. T. Feeley, and C. B. Ma, "The Relationship between Tear Severity, Fatty Infiltration, and Muscle Atrophy in the Supraspinatus," *Journal of Shoulder and Elbow Surgery* 22 (2013): 18–25, https://doi.org/10.1016/j.jse.2011.12.014.

13. C. Wang, Q. Hu, W. Song, W. Yu, and Y. He, "Adipose Stem Cell–Derived Exosomes Decrease Fatty Infiltration and Enhance Rotator Cuff Healing in a Rabbit Model of Chronic Tears," *The American Journal of Sports Medicine* 48 (2020): 1456–1464, https://doi.org/10.1177/0363546520908847.

14. Y. Yang, L. Qiu, X. Gu, et al., "Monitoring Rotator Cuff Muscle Fatty Infiltration Progression by Magnetic Resonance Imaging T1 Mapping: Correlation with Direct Evaluation Findings in Rats," *The American Journal of Sports Medicine* 50 (2022): 1078–1087, https://doi.org/10.1177/03635465211069976.

15. W. Ji, F. Han, X. Feng, et al., "Cocktail-Like Gradient Gelatin/Hyaluronic Acid Bioimplant for Enhancing Tendon-bone Healing in Fatty-infiltrated Rotator Cuff Injury Models," *International Journal of Biological Macromolecules* 244 (2023): 125421, https://doi.org/10.1016/j.ijbiomac.2023.125421.

16. S. Huang, Y. Rao, M. Zhou, et al., "Engineering an Extracellular Matrix-functionalized, Load-bearing Tendon Substitute for Effective Repair of Large-to-massive Tendon Defects," *Bioactive Materials* 36 (2024): 221–237, https://doi.org/10.1016/j.bioactmat.2024.02.032.

17. L. Wang, Y. Liu, Z. Lin, et al., "Durable Immunomodulatory Hierarchical Patch for Rotator Cuff Repairing," *Bioactive Materials* 37 (2024): 477–492, https://doi.org/10.1016/j.bioactmat.2024.03.029.

18. S. Chaudhury, J. S. Dines, D. Delos, R. F. Warren, C. Voigt, and S. A. Rodeo, "Role of Fatty Infiltration in the Pathophysiology and Outcomes of Rotator Cuff Tears," *Arthritis Care & Research* 64 (2012): 76–82, https://doi.org/10.1002/acr.20552.

19. Y. Itoigawa, K. Yoshida, H. Nojiri, et al., "Association of Recurrent Tear after Arthroscopic Rotator Cuff Repair and Superoxide-Induced Oxidative Stress," *The American Journal of Sports Medicine* 49 (2021): 2048–2055, https://doi.org/10.1177/03635465211014856.

20. M. Flück, D. Fitze, S. Ruoss, et al., "Down-Regulation of Mitochondrial Metabolism After Tendon Release Primes Lipid Accumulation in

Rotator Cuff Muscle," *The American Journal of Pathology* 190 (2020): 1513–1529.

21. S. Wang, Z. Yao, X. Zhang, et al., "Energy-Supporting Enzyme-Mimic Nanoscaffold Facilitates Tendon Regeneration Based on a Mitochondrial Protection and Microenvironment Remodeling Strategy," *Advanced Science* 9 (2022): 2202542, https://doi.org/10.1002/advs.202202542.

22. J. Hoeks and P. Schrauwen, "Muscle Mitochondria and Insulin Resistance: a human Perspective," *Trends in Endocrinology & Metabolism* 23 (2012): 444–450, https://doi.org/10.1016/j.tem.2012.05.007.

23. Y. Wang, R. Branicky, A. Noë, and S. Hekimi, "Superoxide Dismutases: Dual Roles in Controlling ROS Damage and Regulating ROS Signaling," *Journal of Cell Biology* 217 (2018): 1915–1928, https://doi.org/10.1083/jcb.201708007.

24. M. Li, J. Chen, W. Wu, Y. Fang, and S. Dong, "Oxidase-Like MOF-818 Nanozyme with High Specificity for Catalysis of Catechol Oxidation," *Journal of the American Chemical Society* 142 (2020): 15569–15574, https://doi.org/10.1021/jacs.0c07273.

25. W. Jing, C. Xiaolan, C. Yu, Q. Feng, and Y. Haifeng, "Pharmacological Effects and Mechanisms of Tannic Acid," *Biomedicine & Pharmacotherapy* 154 (2022): 113561, https://doi.org/10.1016/j.biopha.2022.113561.

26. Y. Zhao, J. Li, L. Liu, et al., "Zinc-Based Tannin-Modified Composite Microparticulate Scaffolds with Balanced Antimicrobial Activity and Osteogenesis for Infected Bone Defect Repair," *Advanced Healthcare Materials* 12 (2023): 2300303, https://doi.org/10.1002/adhm.202300303.

27. J. Li, H. Ke, X. Lei, et al., "Controlled-release Hydrogel Loaded with Magnesium-based Nanoflowers Synergize Immunomodulation and Cartilage Regeneration in Tendon-bone Healing," *Bioactive Materials* 36 (2024): 62–82, https://doi.org/10.1016/j.bioactmat.2024.02.024.

28. C. Ding, J. Min, Y. Tan, et al., "Combating Atherosclerosis with Chirality/Phase Dual-Engineered Nanozyme Featuring Microenvironment-Programmed Senolytic and Senomorphic Actions," *Advanced Materials* 36 (2024): 2401361, https://doi.org/10.1002/adma.202401361.

29. D. Bi, F. Qu, W. Xiao, et al., "Reactive Oxygen Species-Responsive Gel-Based Microneedle Patches for Prolonged and Intelligent Psoriasis Management," *ACS nano* 17 (2023): 4346–4357, https://doi.org/10.1021/acsnano.2c08979.

30. B. Yu, W. Sun, J. Lin, et al., "Using Cu-Based Metal–Organic Framework as a Comprehensive and Powerful Antioxidant Nanozyme for Efficient Osteoarthritis Treatment," *Advanced Science* 11 (2024): 2307798, https://doi.org/10.1002/advs.202307798.

31. J. Feng, H. Gao, L. Zheng, et al., "A Mn-N_3 Single-atom Catalyst Embedded in Graphitic Carbon Nitride for Efficient CO_2 Electroreduction," *Nature Communications* 11 (2020): 4341, https://doi.org/10.1038/s41467-020-18143-y.

32. C. S. Bestwick and N. Maffulli, "Reactive Oxygen Species and Tendinopathy: Do They Matter?," *British Journal of Sports Medicine* 38 (2004): 672–674, https://doi.org/10.1136/bjsm.2004.012351.

33. W. Shi, B. Hass, M. A. Kuss, et al., "Fabrication of Versatile Dynamic Hyaluronic Acid-based Hydrogels," *Carbohydrate Polymers* 233 (2020): 115803, https://doi.org/10.1016/j.carbpol.2019.115803.

34. K.-Y. Lu, P.-Y. Lin, E.-Y. Chuang, et al., "H_2O_2-Depleting and O_2-Generating Selenium Nanoparticles for Fluorescence Imaging and Photodynamic Treatment of Proinflammatory-Activated Macrophages," *ACS applied materials & interfaces* 9 (2017): 5158–5172, https://doi.org/10.1021/acsami.6b15515.

35. N. Piergies, E. Proniewicz, Y. Ozaki, Y. Kim, and L. M. Proniewicz, "Influence of Substituent Type and Position on the Adsorption Mechanism of Phenylboronic Acids: Infrared, Raman, and Surface-enhanced Raman Spectroscopy Studies," *The Journal of Physical Chemistry A* 117 (2013): 5693–5705, https://doi.org/10.1021/jp404184x.

36. B. Hochreiter, C. Germann, G. C. Feuerriegel, et al., "Natural History of Quantitative Fatty Infiltration and 3D Muscle Volume after Nonoperative Treatment of Symptomatic Rotator Cuff Tears: a Prospective MRI Study of 79 Patients," *The Journal of Bone and Joint Surgery American Volume* 106 (2024): 690–699.

37. X. Li, Z. Su, K. Shen, et al., "Eugenol-Preconditioned Mesenchymal Stem Cell-Derived Extracellular Vesicles Promote Antioxidant Capacity of Tendon Stem Cells in Vitro and in vivo," *Oxidative Medicine and Cellular Longevity* 2022 (2022): 3945195, https://doi.org/10.1155/2022/3945195.

38. S. Chen, J. Wang, Y. Chen, X. Mo, and C. Fan, "Tenogenic Adipose-derived Stem Cell Sheets with Nanoyarn Scaffolds for Tendon Regeneration," *Materials Science and Engineering: C* 119 (2021): 111506, https://doi.org/10.1016/j.msec.2020.111506.

39. S. Dex, P. Alberton, L. Willkomm, et al., "Tenomodulin Is Required for Tendon Endurance Running and Collagen I Fibril Adaptation to Mechanical Load," *EBioMedicine* 20 (2017): 240–254, https://doi.org/10.1016/j.ebiom.2017.05.003.

40. C. H. Jo, H.-J. Lim, and K. S. Yoon, "Characterization of Tendon-Specific Markers in Various Human Tissues, Tenocytes and Mesenchymal Stem Cells," *Tissue Engineering and Regenerative Medicine* 16 (2019): 151–159, https://doi.org/10.1007/s13770-019-00182-2.

41. Y. Hu, Z. J. Pan, W. Liao, et al., "Determination of Antioxidant Capacity and Phenolic Content of Chocolate by Attenuated Total Reflectance-Fourier Transformed-infrared Spectroscopy," *Food Chemistry* 202 (2016): 254–261, https://doi.org/10.1016/j.foodchem.2016.01.130.

42. N. Singh, S. K. NaveenKumar, M. Geethika, G. Mugesh, et al., "A Cerium Vanadate Nanozyme with Specific Superoxide Dismutase Activity Regulates Mitochondrial Function and ATP Synthesis in Neuronal Cells," *Angewandte Chemie International Edition* 60 (2021): 3121–3130, https://doi.org/10.1002/anie.202011711.

43. S. Tarafder, J. A. Brito, S. Minhas, L. Effiong, S. Thomopoulos, and C. H. Lee, "In Situ Tissue Engineering of the Tendon-to-bone Interface by Endogenous Stem/Progenitor Cells," *Biofabrication* 12 (2019): 015008, https://doi.org/10.1088/1758-5090/ab48ca.

44. P. Büchler, N. A. Ramaniraka, L. R. Rakotomanana, et al., "A Finite Element Model of the Shoulder: Application to the Comparison of Normal and Osteoarthritic Joints," *Clinical Biomechanics* 17 (2002): 630–639.

45. R. Yang, G. Li, C. Zhuang, et al., "Gradient Bimetallic Ion–based Hydrogels for Tissue Microstructure Reconstruction of Tendon-to-bone Insertion," *Science Advances* 7 (2021): abg3816, https://doi.org/10.1126/sciadv.abg3816.

46. H. Suzuki, Y. Ito, M. Shinohara, et al., "Gene Targeting of the Transcription Factor Mohawk in Rats Causes Heterotopic Ossification of Achilles Tendon via Failed Tenogenesis," *Proceedings of the National Academy of Sciences* 113 (2016): 7840–7845, https://doi.org/10.1073/pnas.1522054113.

47. B. R. Kuzel, S. Grindel, R. Papandrea, and D. Ziegler, "Fatty Infiltration and Rotator Cuff Atrophy," *Journal of the American Academy of Orthopaedic Surgeons* 21 (2013): 613–623, https://doi.org/10.5435/JAAOS-21-10-613.

48. X. Yuan, Y. Zhao, J. Li, et al., "Citrate-based Mussel-inspired Magnesium Whitlockite Composite Adhesives Augmented Bone-to-tendon Healing," *Journal of Materials Chemistry B* 9 (2021): 8202–8210, https://doi.org/10.1039/D1TB01710A.

49. L. J. Rubino, H. F. Stills, D. C. Sprott, and L. A. Crosby, "Fatty Infiltration of the Torn Rotator Cuff Worsens over Time in a Rabbit Model," *Arthroscopy* 23 (2007): 717–722, https://doi.org/10.1016/j.arthro.2007.01.023.

50. L. Miao and D. K. St Clair, "Regulation of Superoxide Dismutase Genes: Implications in Disease," *Free Radical Biology and Medicine* 47 (2009): 344–356, https://doi.org/10.1016/j.freeradbiomed.2009.05.018.

51. Y. Wang, Y. Zhao, S. Ma, et al., "Injective Programmable Proanthocyanidin-Coordinated Zinc-Based Composite Hydrogel for Infected Bone Repair," *Advanced Healthcare Materials* 13 (2024): 2302690, https://doi.org/10.1002/adhm.202302690.

Supporting Information

Additional supporting information can be found online in the Supporting Information section.

Supporting File: adfm75987-sup-0001-SuppMat.doc.